

Calibrated uncertainty quantification for prosumer flexibility aggregation in ancillary service markets

Yogesh Pipada Sunil Kumar^a, S. Ali Pourmousavi^a, Jon A.R. Liisberg^b, Julian Lesmos-Vinasco^b

^a*School of Electrical and Mechanical Engineering, The University of Adelaide, Ingkarni Wardli Building, Adelaide, SA 5005, Australia*

^b*Watts A/S, Brogade 19D, Køge 4600, Denmark*

Abstract

Reliable forecasting of prosumer flexibility is critical for demand response aggregators participating in frequency controlled ancillary service markets, where strict reliability requirements such as the P90 standard are enforced. Limited historical data, dependence on exogenous forecasts, and heterogeneous prosumer behaviour introduce significant epistemic uncertainty, making deterministic or poorly calibrated probabilistic models unsuitable for market bidding. This paper proposes the use of a scalable uncertainty quantification framework that integrates monte carlo dropout (MCD) with conformal prediction (CP) to produce calibrated, finite-sample prediction intervals for aggregated prosumer flexibility.

The proposed framework is applied to a behind-the-meter aggregator participating in the Danish manual frequency restoration reserve capacity market. A large-scale synthetic dataset is generated using a modified industry-grade home energy management system, combined with publicly available load, solar, price, activation, and device-level data. The resulting machine learning surrogate model captures aggregate prosumer price responsiveness and provides uncertainty-aware flexibility estimates suitable for market bidding.

Multiple multivariate conformal prediction strategies are evaluated and benchmarked against conventional MCD-based methods. Results show that standalone MCD systematically overestimates available flexibility and violates P90 compliance, whereas the proposed MCD-CP framework achieves reliable coverage with controlled conservatism. When embedded in an aggregator bidding model, conformalised methods substantially reduce overbidding risk and achieve up to 70% of perfect-information profit while satisfying regulatory reliability constraints, providing a practical, computationally efficient, and market-compliant solution for aggregator flexibility forecasting under uncertainty.

Keywords: aggregator, monte carlo dropout, conformal prediction, prosumer flexibility

1. Introduction

1.1. Motivation

Independent demand response aggregators combine distributed energy resources (DERs) such as photovoltaic systems, residential batteries, electric vehicles, and flexible loads to provide demand side flexibility to energy and balance markets. They act as intermediaries between small scale prosumers, who individually offer limited flexibility, and system

operators, who increasingly depend on fast and affordable flexibility as conventional generation retires. Effective aggregator models can reduce consumer costs, stimulate innovation, and accelerate DER adoption while enhancing system efficiency and supporting grid stability [1]. Aggregators therefore play a pivotal role in enabling a cost effective and resilient energy transition. Hence, the European Union has introduced measures under the Electricity Directive (EU) 2019/944 [2] and the Electricity Regulation (EU) 2024/1747 [3] to ensure equitable participation of aggregators in electricity markets. These initiatives, complemented by ongoing consultations on a demand response network code [4], aim to remove regulatory barriers and strengthen the operational and market integration of aggregators across Europe.

One of the central challenges in aggregator business models is predicting prosumer price responsiveness, that is, the extent of flexibility offered at a given incentive level and a given time. This relationship is inherently complex, as prosumer behaviour depends on interdependent factors such as weather, load variability, solar generation, and behavioural inconsistencies [5, 6]. Data-driven models have therefore emerged as an effective solution, enabling accurate and scalable estimation of prosumer behaviour from historical data without restrictive assumptions [7]. However, the limited availability of behavioural data and the reliance on forecasts of weather, load, solar generation, and price introduce significant epistemic uncertainty into these models. Such uncertainty directly affects the procurement and delivery of critical balancing services, where reserved capacity may not be available when required.

From an economic perspective, enforcing 100% availability requirements on aggregators relying on inherently uncertain flexibility sources would impose excessive financial risk, potentially rendering participation unprofitable and discouraging market entry. To balance the risk of capacity unavailability with the need to incentivise aggregator participation, the Danish system operator has adopted a P90 compliance standard for frequency controlled ancillary services (FCAS) capacity market participants, allowing a capacity deviation with a maximum probability of 10% [8]. Non-compliance can result in financial penalties or suspension from market participation, highlighting the need for predictive models with integrated uncertainty quantification. Consequently, this study aims to develop a data-driven framework that captures epistemic uncertainty while providing formal coverage guarantees, thus improving the robustness of aggregator forecasts under data scarcity and market reliability constraints.

1.2. Related work

Uncertainty quantification (UQ) has become a central research focus in energy forecasting, particularly for aggregator business models that depend on reliable flexibility estimation under limited data availability and forecast dependence. Probabilistic models that capture both aleatoric and epistemic uncertainties enable more informed and risk-aware decision-making, aligning with regulatory requirements such as the P90 compliance standard in ancillary service markets.

Bayesian neural networks (BNNs) have been widely studied for demand and flexibility forecasting due to their ability to capture both epistemic and aleatoric uncertainty by learning distributions over model parameters [9]. Several studies report improved uncertainty quantification for residential demand forecasting using BNNs compared to deterministic neural networks [10, 11, 12]. More recently, [13] applied a BNN-based transformer architecture to electric vehicle flexibility forecasting for frequency regulation markets, demonstrating strong predictive performance. However, the high computational

cost of BNNs limits their scalability, particularly for complex architectures and longer forecasting horizons.

Approximate Bayesian methods such as Monte Carlo dropout (MCD) provide a computationally efficient alternative [14, 15]. By retaining dropout layers during inference, MCD produces a predictive distribution that can be interpreted as an approximation of a deep Gaussian process [15]. This approach has been applied successfully in medical imaging [16], object detection [17], and energy demand forecasting [18]. Nonetheless, MCD does not yield a true Bayesian posterior and can result in miscalibrated uncertainty estimates, particularly in multi-output or long-horizon settings [19, 20].

To address calibration issues, a promising research direction is the integration of MCD with conformal prediction (CP) as proposed by authors in [21]. CP provides a lightweight and distribution-free framework to obtain prediction intervals with finite-sample coverage guarantees under data exchangeability [22, 23]. Applications in electricity price [24] and photovoltaic generation forecasting [25] commonly employ conformalised quantile regression, where quantile regression is combined with CP to obtain calibrated prediction quantiles. However, such approaches primarily address aleatoric uncertainty and are less effective in settings dominated by epistemic uncertainty [26]. This limitation is particularly pronounced in prosumer flexibility forecasting, where epistemic uncertainty arises from limited training data and dependence on exogenous forecasts such as weather conditions and market prices. While quantile regression struggles to represent this uncertainty, MCD is well suited to capturing epistemic effects but often produces miscalibrated intervals. The hybrid integration of MCD and CP therefore offers a complementary solution, combining epistemic uncertainty representation with calibrated prediction intervals and finite-sample guarantees [21].

Despite its potential, this hybrid approach has not yet been investigated for prosumer flexibility forecasting or aggregator bidding problems. Moreover, existing applications of MCD and CP have largely been restricted to single-output settings, whereas aggregator decision-making requires multivariate, multi-time-step predictions. Although multivariate CP is an emerging area of research [27], its integration with MCD in energy market applications remains unexplored, highlighting a clear methodological gap addressed by this work.

1.3. Contributions

In this study we implement a framework based on MCD-CP uncertainty quantification (UQ) to model the price responsiveness of prosumers for an aggregator participating in the European FCAS markets. A decision-dependent chance-constrained optimisation program was developed to simulate the aggregator’s bidding problem under uncertainty. To enable a realistic evaluation, a synthetic dataset was generated using a modified version of the industry-grade home energy management system (HEMS) algorithm from Watts A/S [28], combined with publicly available datasets for load and solar profiles, market prices, activation data, and device-level size distributions of residential batteries and solar panels. The proposed framework was trained and assessed for both P90 compliance and economic performance.

The main contributions of this work relative to the aggregator operation state-of-the-art (SOTA) are as follows:

1. In contrast to prior studies that rely on computationally expensive BNNs and are largely restricted to short-term settings [10, 11, 12, 13], this work proposes the use

of the hybrid MCD–CP framework introduced in [21] for a multi-time-step, multivariate aggregator bidding problem. The results demonstrate that the proposed approach can reliably satisfy the P90 compliance requirement while remaining economically viable in the Danish FCAS capacity market.

2. Unlike existing applications of MCD [18] or CP [25, 24], which predominantly address single-output forecasting tasks, this study systematically deploys and compares standalone MCD and hybrid MCD–CP methods within a realistic multi-step aggregator optimisation problem. The results show that the miscalibration inherent to standalone MCD can be effectively mitigated through conformal calibration, yielding prediction intervals that are both statistically reliable and suitable for market-based decision-making.
3. We develop a large-scale synthetic dataset using a modified industry-grade HEMS algorithm from Watts A/S, combined with publicly available datasets for load and solar profiles, market prices, activation signals, and residential device size distributions. This enables a realistic evaluation of both predictive reliability and economic performance under real-world market conditions.

The remainder of this paper is structured as follows. Section 2 formulates the aggregator bidding optimisation problem. Section 3 introduces the hybrid MCD–CP framework. Section 4 outlines the case study setup, data generation strategy, and the learning architecture. Section 5 presents and discusses the results, and Section 6 concludes the study with key findings and future directions.

2. Aggregator business model

This section presents the business model of the behind-the-meter flexibility aggregator and outlines the associated mathematical framework considered in this study.

2.1. Background and context

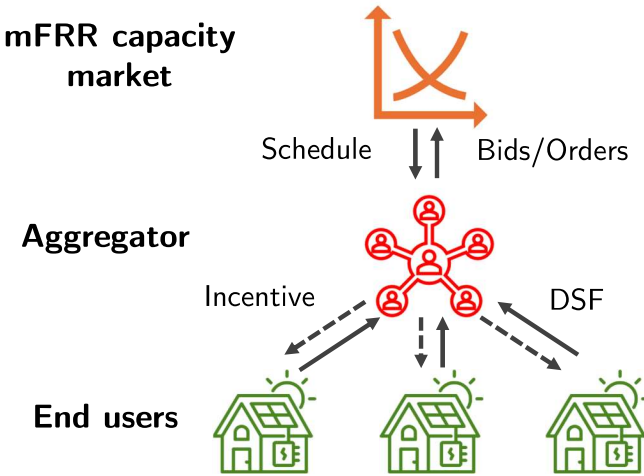


Figure 1: Aggregator business model

In this study, we consider the operation of a behind-the-meter flexibility aggregator participating in the Danish manual frequency restoration reserve (mFRR) capacity market. Figure 1 illustrates the framework based on indirect load-control adopted in this case

study. The aggregator sends incentive price signals to the HEMS of multiple prosumers, who voluntarily adjust their consumption to provide flexibility. This aggregated flexibility is traded by the aggregator in relevant electricity markets and services. Although market structures vary between regions, the analysis focuses on the Danish mFRR capacity market operated by Energinet. Nevertheless, the proposed mathematical framework is adaptable to similar market mechanisms, such as automatic frequency regulation reserves markets.

The Danish mFRR capacity market procures tertiary reserves through a pay-as-clear, day-ahead auction, securing reserve commitments for the subsequent delivery day. The market is asymmetric, allowing participants to offer up-regulation, down-regulation, or both. Up-regulation corresponds to increased generation or reduced consumption, while down-regulation involves increased consumption or reduced generation. Accepted capacity bids are remunerated at the market-clearing price irrespective of activation, subject to reserve availability. Participation is governed by Energinet's P90 reliability requirement, which permits reserve shortages or overbidding with a maximum probability of 10%. Actual energy delivery is coordinated through the mFRR activation market, operated 45 minutes before delivery using a pay-as-clear mechanism with one-price imbalance settlement. More details on Danish ancillary service markets and regulatory frameworks are available in [29, 30].

2.2. Assumptions and mathematical framework

Based on the background and context presented in Section 2.1, the aggregator's bidding framework requires a flexibility prediction algorithm capable of estimating the flexibility available under the varying incentive profiles offered to prosumers. Furthermore, this prediction model must be embedded within the bidding optimisation problem of the aggregator, where the incentive profile offered to all prosumer's HEMS is treated as a decision variable. Finally, to satisfy the P90 reliability criterion, the bidding formulation must adopt a chance-constrained programming approach. Consequently, the following assumptions are made to formulate the aggregator's profit maximisation problem.

- The aggregator is a price-taking entity that participates in the mFRR capacity market. It has access to point predictions of mFRR up- and down-regulation market prices and mFRR up- and down-regulation reserve activation forecasts, which are used within its decision-making algorithms.
- Distribution grid related constraints, such as congestion, are ignored within this framework. However, the model can be adapted to account for the same.
- The available up- and down-flexibility of the prosumer cluster is uncertain and are characterised using probabilistic forecast models. These models are further described in Section 3.

Let $\mathcal{T} = \{1, \dots, T\}$ denote the set of time intervals considered in the optimisation horizon, where $T \in \mathbb{N}$. The price profiles of the mFRR capacity market for up- and down-regulation are indicated by $\boldsymbol{\lambda}^U, \boldsymbol{\lambda}^D \in \mathbb{R}^T$ (DKK/MWh), while $\boldsymbol{\lambda}^B \in \mathbb{R}^T$ represents the imbalance price profile of the mFRR activation market (DKK/MWh). The corresponding activation signals from Energinet are represented by $\boldsymbol{a}^\uparrow, \boldsymbol{a}^\downarrow \in [0, 1]^T$. Let $\boldsymbol{x}^u, \boldsymbol{x}^d \in \mathbb{R}_+^T$ denote the reserved up- and down-regulation flexibility (MWh), and $\boldsymbol{\lambda}^{I,u}, \boldsymbol{\lambda}^{I,d} \in \mathbb{R}_+^T$ the incentive price profiles offered to the prosumer group (DKK/MWh) to provide up- and

down-flexibility, respectively. The random vectors $\mathbf{y}^u, \mathbf{y}^d \in \mathbb{R}_+^T$ represent the maximum up- and down-flexibility available from the prosumer group (MWh). Finally, let $\mathcal{F}(\mathbf{y}^u, \mathbf{y}^d)$ denote a statistical or probabilistic measure associated with these random variables, such as the cumulative distribution function or relevant quantiles. Thus, the aggregator's bidding optimisation problem can be formulated as follows.

$$\max_{\mathcal{X}} \sum_{t \in \mathcal{T}} \left[\left(\lambda_t^u + a_t^\uparrow \lambda_t^B - \lambda_t^{I,u} \right) x_t^u + \left(\lambda_t^d - a_t^\downarrow \lambda_t^B - \lambda_t^{I,d} \right) x_t^d \right] \quad (1a)$$

$$\text{s.t. } \mathbb{P}(x_t^i \leq y_t^i, \forall t \in \mathcal{T}) \geq 1 - \alpha \quad \forall i \in \{u, d\} \quad (1b)$$

$$\mathcal{F}(\mathbf{y}^u, \mathbf{y}^d) = \Phi(\boldsymbol{\lambda}^{I,u}, \boldsymbol{\lambda}^{I,d}, \boldsymbol{\zeta}) \quad (1c)$$

The set of decision variables is defined as $\mathcal{X} = \{x^u, \boldsymbol{\lambda}^{I,u}, \mathbf{y}^u, x^d, \boldsymbol{\lambda}^{I,d}, \mathbf{y}^d\}$. Equation (1a) represents the aggregator's profit function, while Equation (1b) introduces a joint chance constrained that enforces the availability requirement of Energinet's P90 on the offered bid capacity. The statistical characteristics of the random variables $\mathcal{F}(\mathbf{y}^u, \mathbf{y}^d)$ are modelled using a data-driven algorithm denoted by $\Phi(\cdot)$, as shown in Eq. (1c). Thus, the optimisation model is a decision-dependent chance-constrained program, as it captures the influence of incentive prices offered to prosumers, $\boldsymbol{\lambda}^{I,u}$ and $\boldsymbol{\lambda}^{I,d}$ on the uncertain parameters. Moreover, it incorporates contextual information $\boldsymbol{\zeta}$, such as forecasts of load, solar generation, retailer prices, market activation signals, and aggregated data from prosumer devices. It is important to note that this optimisation problem is solved by the aggregator, not by individual prosumers' HEMS. Though, the focus of this study is mFRR markets, this optimisation framework can easily be extended to other Danish FCAS markets.

The proposed optimisation model simultaneously determines the bid submitted to the mFRR market and the incentive offered to prosumers. Consequently, the objective function is bilinear. Owing to this bilinear structure and the potentially nonlinear nature of the probabilistic flexibility model, the resulting optimisation problem is non-convex, and subsequently computationally challenging to solve. To improve tractability, prosumer incentive prices are treated as fixed parameters rather than decision variables. This removes bilinear terms from the objective and allows flexibility estimates to be obtained externally via an estimator $\Phi_{1-\alpha}(\boldsymbol{\lambda}^{I,u}, \boldsymbol{\lambda}^{I,d}, \boldsymbol{\zeta}) = (\hat{\mathbf{y}}^u, \hat{\mathbf{y}}^d)$, where $\hat{\mathbf{y}}^u, \hat{\mathbf{y}}^d \in \mathbb{R}^T$ are calibrated to satisfy the chance constraint in Eq. (1b). The optimisation is evaluated over multiple incentive-price scenarios, and the most profitable case is selected.

Logically, incentive prices must remain below market clearing prices for aggregator to be profitable. A proportional revenue-sharing mechanism is therefore adopted, where $\beta \in [0, 1]$ denotes the fraction of market revenue allocated to prosumers. Discretising β yields a finite set of incentive scenarios \mathcal{S}_β . The resulting linearised optimisation model is presented in Eqs. (2a)–(2b).

$$\max_{\mathcal{X}} \sum_{t \in \mathcal{T}} \left[\left(\lambda_t^u + a_t^\uparrow \lambda_t^B - \lambda_t^{I,u} \right) x_t^u + \left(\lambda_t^d - a_t^\downarrow \lambda_t^B - \lambda_t^{I,d} \right) x_t^d \right] \quad (2a)$$

$$\text{s.t. } x_t^i \leq \hat{y}_t^i, \quad \forall t \in \mathcal{T}, \forall i \in \{u, d\} \quad (2b)$$

$$\lambda_t^{I,u} = \beta \left(\lambda_t^u + a_t^\uparrow \lambda_t^B \right) \quad \forall t \in \mathcal{T} \quad (2c)$$

$$\lambda_t^{I,d} = \beta \left(\lambda_t^d - a_t^\downarrow \lambda_t^B \right) \quad \forall t \in \mathcal{T} \quad (2d)$$

The resulting simplified problem is straightforward to solve, allowing the aggregator to efficiently assess multiple incentive pricing scenarios and identify the one that maximises profit. However, by fixing incentive prices *ex ante* and decoupling them from the flexibility predictor $\Phi_{1-\alpha}(\cdot)$ within the optimisation, the identified maximum profit solution becomes inherently sub-optimal. The extent of this sub-optimality depends on the resolution and number of scenarios considered, reflecting a deliberate trade-off between computational tractability and solution optimality. While a revenue-sharing incentive mechanism is adopted in this study, the proposed optimisation framework is sufficiently general to support alternative incentive design strategies.

3. Methodology

3.1. Uncertainty quantification framework

In this section, we describe the UQ framework used in this study to capture uncertainty in the behaviour of prosumers, that is, the flexibility prediction algorithm $\Phi_{1-\alpha}(\cdot)$. As noted earlier, the prediction made by the algorithm should guarantee satisfaction of the joint chance constrained. As introduced in Section 1, A hybrid MCD and CP method is used to achieve this.

Traditionally, dropout layers in neural networks (NNs) are used to prevent overfitting by probabilistically “switching off” neurons during training using a user-defined dropout rate. These layers are typically disabled during inference. However, [15] showed that a NN with dropout across all weight layers can be viewed as a probabilistic deep Gaussian process. By retaining dropout during inference and performing multiple stochastic forward passes, one can approximate samples from a deep Gaussian process. This approach, known as MCD, offers a scalable and computationally efficient alternative to BNNs, especially when the uncertainty structure is not highly complex. On the other hand, CP is a distribution-free framework for uncertainty quantification that constructs statistically valid prediction sets under the assumption of data exchangeability [22, 23]. It is simple, model-agnostic, and computationally efficient. Among its variants, this study adopts the split CP.

Being a “Bayesianesque” approximation, NN with MCD effectively captures epistemic (model-related) uncertainty [15], though it may exhibit poor calibration for complex posteriors. Integrating it with CP enhances uncertainty reliability while retaining tractability. Moreover, the marginal coverage guarantee of CP allows the multivariate prediction region ξ to be interpreted as element-wise upper and lower bounds that satisfy joint chance constraints, which makes this hybrid framework well-suited to our application. The Algorithm 1 defines the probabilistic prediction framework $\Phi_{1-\alpha}(\cdot)$ used for uncertainty quantification. Various conformity scores can be adopted for multivariate predictions; see [27] for details. The scores used in this study are specified in Section 3.2.

Marginal coverage ensures that, on average, the prediction region contains the true output with probability $1 - \alpha$, though not necessarily for each individual input (conditional coverage). Thus, while some samples may be over- or under-covered, the expected coverage remains correct [31]. Although conditional coverage is generally unattainable without distributional assumptions, marginal coverage can be interpreted to yield conservative element-wise bounds on \mathbf{y} , as shown in Eqs. (3)–(5), where $\mathbf{u} = \sup \xi$ and $\mathbf{l} = \inf \xi$.

$$\mathbb{P} [\mathbf{y} \in \xi] \geq 1 - \alpha \quad (3)$$

Algorithm 1 Hybrid MCD and split CP for obtaining multivariate prediction intervals

Require: NN with dropout layers f_y trained on $\mathcal{D}_{\text{train}}$, number of MC samples S , calibration set \mathcal{D}_{cal} , new input $\Theta \not\subset \mathcal{D}_{\text{train}} \cup \mathcal{D}_{\text{cal}}$, coverage level $1 - \alpha$

Ensure: Prediction set ξ

CP calibration:

- 1: Initialise calibration score vector $\mathbf{q} \in \mathbb{R}^{|\mathcal{D}_{\text{cal}}|+1}$
- 2: **for** $j = 1$ to $|\mathcal{D}_{\text{cal}}|$ **do**
- MCD algorithm start**
- 3: Set model f_y to **train mode** to activate dropout at inference
- 4: Initialise prediction matrix $\mathbf{Y}^{(j)} \in \mathbb{R}^{S \times d}$ where d is the output dimension
- 5: **for** $i = 1$ to S **do**
- 6: $\hat{\mathbf{y}}^{(i)} \leftarrow f_y(\Theta^{(j)}) \in \mathbb{R}^d$ ▷ Vector output
- 7: Store $\hat{\mathbf{y}}^{(i)}$ as row i in matrix $\mathbf{Y}^{(j)}$
- 8: **end for**
- MCD algorithm end**
- 9: $q_j \leftarrow s(\mathbf{Y}^{(j)}, \mathbf{y}^{(j)}) \in \mathbb{R}$
- 10: **end for**
- 11: Compute the adjusted quantile level:

$$\hat{\alpha} = \frac{\lceil (|\mathcal{D}_{\text{cal}}| + 1)(1 - \alpha) \rceil}{|\mathcal{D}_{\text{cal}}| + 1}$$

- 12: Compute the $\hat{\alpha}$ quantile of the calibration scores:

$$\hat{q} = \text{Quantile}_{\hat{\alpha}}(\mathbf{q} \cup \{\infty\}) \in \mathbb{R}$$

CP Inference:

- 13: For a new random input Θ , compute MCD sample predictions $\mathbf{Y} \in \mathbb{R}^{S \times d}$ using steps 3 – 8
- 14: Construct the prediction region of the output \mathbf{y} as:

$$\xi = \{\mathbf{y} \in \mathbb{R}^d : s(\mathbf{Y}, \mathbf{y}) \leq \hat{q}\}$$

- 15: **return** ξ

$$\mathcal{B}_\xi = \{\mathbf{y} \in \mathbb{R}^d \mid \mathbf{l} \leq \mathbf{y} \leq \mathbf{u}\} \tag{4}$$

$$\therefore \mathbb{P}[\mathbf{y} \in \mathcal{B}_\xi] \geq \mathbb{P}[\mathbf{y} \in \xi] \geq 1 - \alpha \tag{5}$$

Figure 2 illustrates this concept, where a bounding hyperrectangle \mathcal{B}_ξ encloses the conformal prediction region ξ . By construction, $\mathbb{P}[\mathbf{y} \in \mathcal{B}_\xi] \geq 1 - \alpha$. These conservative bounds are particularly advantageous for downstream optimisation problems involving joint chance constraints, such as those defined in Eqs. (1a)–(1c). For example, in a chance-constrained optimisation problem with decision variables $\mathbf{x} \in \mathbb{R}^d$ and random vector \mathbf{y} as defined above, the probabilistic constraint $\mathbb{P}[x_i \leq y_i, \forall i \in \{1, \dots, d\}] \geq 1 - \alpha$ can be conservatively reformulated as the deterministic constraint $\mathbf{x} \leq \mathbf{l}$. Similarly, the probabilistic constraint $\mathbb{P}[x_i \geq y_i, \forall i \in \{1, \dots, d\}] \geq 1 - \alpha$ can be conservatively reformulated as the deterministic constraint $\mathbf{x} \geq \mathbf{u}$.

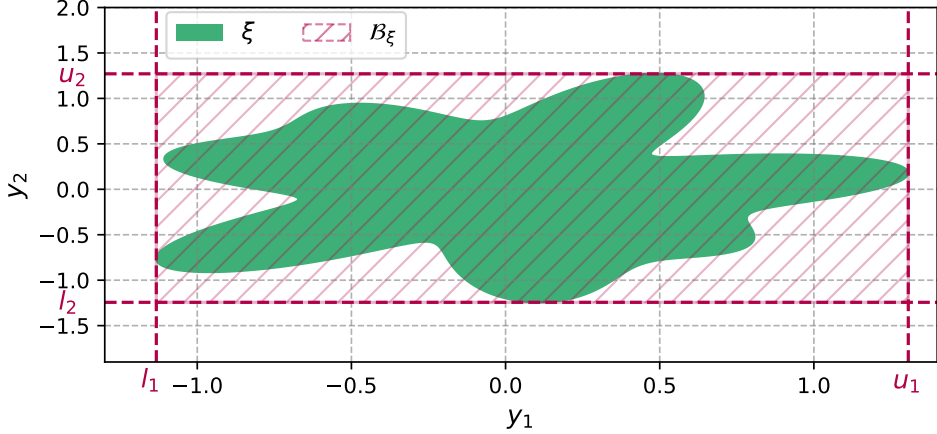


Figure 2: Example conformal prediction region ξ for $\mathbf{y} \in \mathbb{R}^2$ with bounding rectangle \mathcal{B}_ξ

3.2. Conformity scores

As discussed in Section 3.1, the choice of the conformity score critically influences the quality and geometry of the multivariate prediction intervals generated by the proposed UQ framework (Algorithm 1). Assuming the dataset is exchangeable, any conformal prediction method guarantees marginal coverage; however, maintaining narrow prediction intervals may be essential to maximise downstream profitability.

This section evaluates three conformity metrics within the split CP framework (Algorithm 1), along with a copula-based CP approach commonly used in multivariate forecasting. Other conformity measures, such as those based on cumulative distributions or latent representations, are beyond the present scope but are discussed in [27]. The MCD approach can be integrated with any of these methods, highlighting its flexibility in generating diverse statistical representations as precursors to CP. The notation of Algorithm 1 is retained, with subscripts used to distinguish the prediction regions for each metric.

The first conformity metric, termed multivariate conformal prediction (MCP), follows [27, 32]. Quantiles derived from MCD-based predictions are calibrated using the conformity score defined in [27], and the corresponding conformalised prediction interval ξ_{MCP} is obtained using Eq. (6).

$$\xi_{MCP} = \times_{t=1}^d [\mathcal{Q}_t(\mathbf{Y}, \alpha) - \hat{q}, \mathcal{Q}_t(\mathbf{Y}, 1 - \alpha) + \hat{q}] \quad (6)$$

Here, $\mathcal{Q}_t(\cdot, \tau)$ denotes the τ -quantile of the predicted samples at index t . The conformity score measures the maximum deviation of the true output from the predicted quantile band. Since the α to $1 - \alpha$ quantile interval inherently provides coverage of $1 - 2\alpha$, Algorithm 1 calibrates \hat{q} to achieve this target coverage, i.e., $\mathbb{P}[\mathbf{y} \in \xi_{MCP}] \geq 1 - 2\alpha$. Although the lower bound $\inf \xi_{MCP}$ is expected to satisfy $\mathbb{P}[\mathbf{y} \geq \inf \xi_{MCP}] \geq 1 - \alpha$, this may not always hold in practice, making MCP less conservative than other approaches and potentially non-compliant with the P90 standard (see Section 5.1).

The second metric is based on the univariate problem specified in [33], which we generalised to a multivariate setting. It uses the univariate Mahalanobis distance to quantify the deviation of the true output from the predictive mean obtained from MCD samples, expressed in units of the sampled standard deviation. The corresponding prediction interval is defined as the predictive mean plus or minus a scaled deviation, as shown in

Eq. (7d).

$$\mu_t^{(j)} = \frac{1}{S} \sum_{i=1}^S Y_{i,t}^{(j)} \quad \forall t \in \{1, \dots, d\} \quad (7a)$$

$$\sigma_t^{(j)} = \sqrt{\frac{1}{S} \sum_{i=1}^S \left[Y_{i,t}^{(j)} - \mu_t^{(j)} \right]^2} \quad \forall t \in \{1, \dots, d\} \quad (7b)$$

$$s_{MMCP}(\mathbf{Y}^{(j)}, \mathbf{y}^{(j)}) = \max_t \left\{ \frac{y_t^{(j)} - \mu_t^{(j)}}{\sigma_t^{(j)}} \right\} \quad (7c)$$

$$\xi_{MMCP} = \times_{t=1}^d [\mu_t - \hat{q} \cdot \sigma_t, \mu_t + \hat{q} \cdot \sigma_t] \quad (7d)$$

We refer to this conformity score as max-Mahalonobis conformal prediction (MMCP), which computes Mahalanobis distances independently for each output and retains the maximum distance across all outputs. This yields an axis-aligned hyperrectangular prediction region ξ_{MMCP} , equivalent to its bounding box $\mathcal{B}\xi_{MMCP}$. The calibration threshold \hat{q} is obtained using Algorithm 1 for coverage $1 - \alpha$, using $\boldsymbol{\mu}$ and $\boldsymbol{\sigma}$ from (7a)–(7b) and the conformity score presented in Eq. (7c).

The third metric, termed probabilistic conformal prediction (PCP) and proposed in [34], determines the radius of the smallest hypersphere enclosing the true output, with each predicted sample from the MCD sample serving as a centre, as shown in Eq. (8).

$$\xi_{PCP} = \bigcup_{i \in \mathcal{S}} \{y : \|\mathbf{y} - \mathbf{Y}_i\|_2 \leq \hat{q}\} \quad (8)$$

The prediction region comprises a union of hyperspheres of radius \hat{q} , where \hat{q} is the calibrated conformity score for coverage $1 - \alpha$. The corresponding axis-aligned bounding hyperrectangle is typically the most conservative among all methods.

The final method, copula conformal prediction (CCP), extends the copula-based approach of [35], originally developed for multi-step time series forecasting. Instead of the split CP assumption of independence, this method models joint residual dependencies using copulas, improving the representation of temporal and inter-dimensional correlations. The calibration yields a vector of thresholds $\hat{\mathbf{q}}_{CCP} \in \mathbb{R}^T$ that define the prediction region:

$$\xi_{CCP} = \times_{t=1}^d [\mu_t - \hat{q}_{CCP,t}, \mu_t + \hat{q}_{CCP,t}] \quad (9)$$

Here, the conformity score is the absolute deviation between the true value and sample predictive mean from MCD. Each dimension is independently calibrated using the corresponding element of $\hat{\mathbf{q}}_{CCP}$, which produces a hyperrectangular prediction region ξ_{CCP} equivalent to its bounding box $\mathcal{B}\xi_{CCP}$. The implementation follows the official repository in [36].

As shown in Fig. 3, the bounding box of the PCP method provides a conservative approximation, whereas for MCP, MMCP, and CCP, the bounding box coincides with the prediction region.

4. Case study

This section outlines the simulation case study and the methodology adopted for training the probabilistic prediction algorithm $\Phi_{1-\alpha}$.

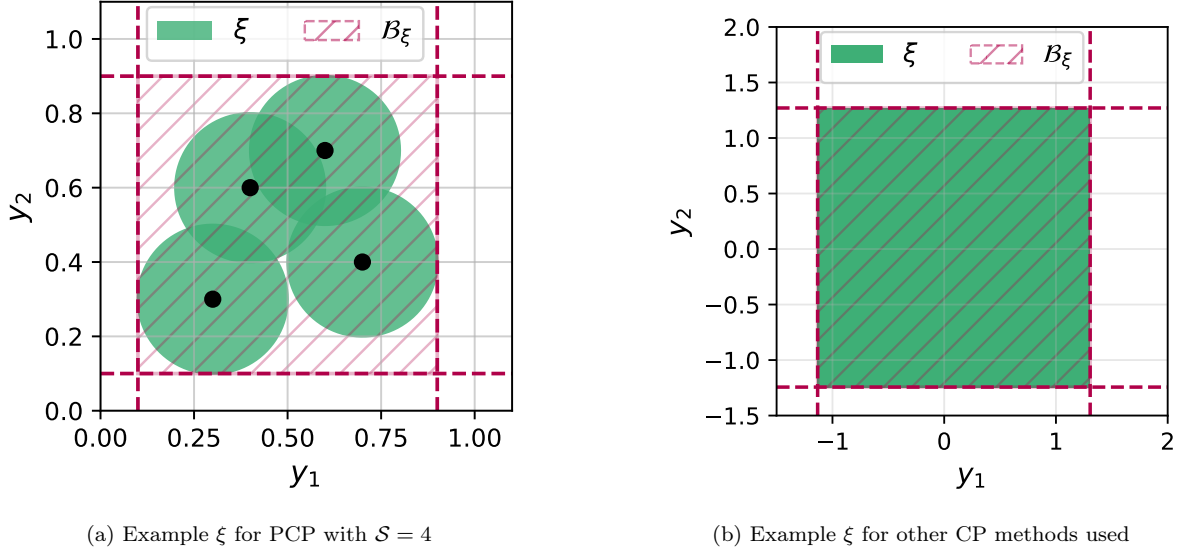


Figure 3: Illustration of prediction regions ξ and corresponding bounding hyperrectangles for $\mathbf{y} \in \mathbb{R}^2$, covering all CP methods evaluated.

The prosumer behaviour is governed by a HEMS scheduling algorithm originally developed by the project’s industry partner, Watts A/S, as detailed in [37]. This baseline HEMS algorithm was subsequently modified to allow participation in the mFRR up-regulation capacity market. As the algorithm is proprietary, its complete formulation cannot be disclosed. However, its essential characteristics and underlying assumptions in addition to those mentioned in [37] are summarised as follows:

1. Each prosumer in the aggregator’s portfolio is equipped with a photovoltaic (PV) system and a residential battery operated by a HEMS algorithm (Watts’ Homegrid ® [38]), with all relevant nameplate parameters known to the aggregator. Additionally, the aggregator uses predictive models that generate point forecasts for the aggregated prosumer electric load and solar generation.
2. All prosumers are subject to an hourly electricity price in real time (Tariff “C”). Under this tariff, prosumers receive the day-ahead market prices when exporting energy to the grid, while energy imports are priced by adding the retailer’s premium, grid tariffs and VAT to the day-ahead market price. The aggregator is assumed to have access to point forecasts of these prices.
3. Flexibility is provided exclusively by the prosumer’s battery. During periods reserved for capacity provision, the battery is scheduled to remain idle; thus, any deviation from this idle state indicates an external activation signal, which can be used to confirm the delivery of service.
4. The current HEMS configuration supports participation only in the mFRR up-regulation capacity market and hence this study is restricted to the same. Furthermore, it uses deterministic forecasts for activation signals and electricity prices, without explicitly accounting for uncertainty.
5. In case of reserve activation, prosumers are remunerated solely by the aggregator for their flexibility. The corresponding load deviation does not affect the electricity bill from the retailer, reflecting a regulatory assumption that dual compensation from both the aggregator and the retailer may be disallowed in the future.

Since the HEMS supports only mFRR up-regulation capacity market participation,

the aggregator's participation is likewise limited to this market. This choice is motivated by the substantially higher average hourly procurement volume in the up-regulation market between August 2023 and April 2025, which is approximately 390 MW, compared to only 35 MW for down-regulation in Denmark as obtained from [39]. This market-specific constraint does not limit the applicability of the UQ framework introduced in Section 3.1, which remains generalisable to other FCAS market formulations. However, it directly affects the bidding optimisation model of the aggregator, as described in Section 2, and is incorporated in Eqs. (10a) and (10b). The prediction region ξ is derived using the proposed UQ framework described in Section 3, ensuring that $\mathbb{P}[\mathbf{y}^u \in \xi] \geq 1 - \alpha$, with $\mathbf{l} = \inf \xi$.

$$\max_{\mathbf{x}} \quad \sum_{t \in \mathcal{T}} (1 - \beta) \lambda_t^U x_t^u \quad (10a)$$

$$\text{s.t.} \quad x_t^u \leq l_t, \quad \forall t \in \mathcal{T} \quad (10b)$$

Finally, the modified Watts HEMS algorithm is employed to generate synthetic data representing aggregated prosumer behaviour. This dataset forms the basis for training the probabilistic prediction model, $\Phi_{1-\alpha}(\cdot)$, using Algorithm 1. It should be emphasised that the model aims to capture the aggregate flexibility of a population of prosumers, rather than individual household behaviour.

4.1. Data generation for training $\Phi_{1-\alpha}(\cdot)$

The input data for the HEMS are categorised into common inputs at the cluster-level and individual prosumer-specific inputs. The common inputs comprise the predicted daily electricity purchase and sale price profiles, $\boldsymbol{\lambda}^P, \boldsymbol{\lambda}^S \in \mathbb{R}^T$ (DKK/kWh), the predicted mFRR up-regulation activation signal, $\mathbf{a}^\uparrow \in \{0, 1\}^T$, and a common up-regulation incentive price offered by the aggregator, $\boldsymbol{\lambda}^{I,u} \in \mathbb{R}^T$. Although fractional activations would more accurately represent partial reserve deployment, the activation signal is modelled as binary in this study due to data availability constraints. Let \mathcal{I} denote the set of prosumers. For each prosumer $i \in \mathcal{I}$, the individual inputs include the predicted daily load and solar generation profiles, $\mathbf{x}^{l,i}, \mathbf{x}^{s,i} \in \mathbb{R}^T$ (kWh), and the battery specifications, characterised by the maximum discharge power $b^{dis,i} \in \mathbb{R}^+$ (kW) and the energy capacity $b^{cap,i} \in \mathbb{R}^+$ (kWh). Accordingly, the input set for the HEMS of prosumer i is defined as $\Theta^i = \{\boldsymbol{\lambda}^P, \boldsymbol{\lambda}^S, \mathbf{a}^\uparrow, \boldsymbol{\lambda}^{I,u}, \mathbf{x}^{l,i}, \mathbf{x}^{s,i}, b^{dis,i}, b^{cap,i}\}$. Based on this input set, the HEMS determines the daily up-regulation capacity reserved by prosumer i , denoted by $\mathbf{y}^{u,i} \in \mathbb{R}^T$ (kW).

The aggregator is primarily interested in the collective response of the prosumer cluster rather than individual HEMS decisions. Consequently, the inputs to the proposed machine learning (ML) model mirror those of the HEMS, with load profiles and battery specifications aggregated across all prosumers. Individual quantities are summed to form cluster-level inputs, and the same aggregation is applied to the outputs, producing a single daily mFRR up-regulation capacity reservation profile. The input to the ML model is therefore defined as $\Theta = \{\boldsymbol{\lambda}^P, \boldsymbol{\lambda}^S, \mathbf{a}^\uparrow, \boldsymbol{\lambda}^{I,u}, \mathbf{x}^{l,agg}, \mathbf{x}^{s,agg}, b^{dis,agg}, b^{cap,agg}\}$, where the superscript “agg” denotes quantities aggregated over all prosumers. The corresponding output is the aggregated daily mFRR up-regulation capacity reservation profile, denoted by $\mathbf{y} = \mathbf{y}^{u,agg}$.

Figure 4 illustrates the data generation workflow used to construct the training dataset to learn the aggregated behaviour of the HEMS. The process begins with the collection of data from relevant sources, including electricity market prices, retail tariffs, and mFRR

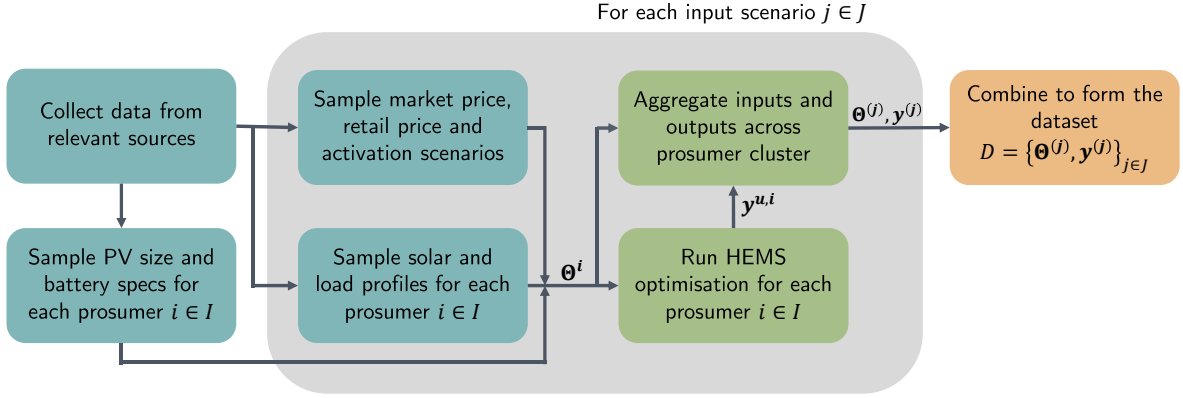


Figure 4: Synthetic data generation framework

activation signals. Prosumer-specific technology characteristics, namely photovoltaic system sizes and battery specifications, are sampled once for each prosumer $i \in \mathcal{I}$ and remain fixed across all scenarios, representing a static physical asset configuration. In contrast, market price trajectories, activation patterns, and daily load and solar generation profiles are sampled on a per-scenario basis to capture temporal and market-driven variability. For each scenario, these quantities are combined to form individual HEMS input sets Θ^i .

Given these inputs, the HEMS optimisation problem is solved independently for each prosumer, resulting in the corresponding daily up-regulation capacity reservation $\mathbf{y}^{u,i}$. Individual inputs and outputs are then aggregated across the prosumer cluster: load profiles, solar generation, and battery parameters are summed to form the input at the cluster-level Θ , while individual capacity reservations are aggregated to produce the corresponding output at the cluster-level $\mathbf{y} = \mathbf{y}^{u,agg}$. Repeating this procedure across multiple sampled scenarios indexed by $j \in \mathcal{J}$ results in the dataset $\mathcal{D} = \{(\Theta^{(j)}, \mathbf{y}^{(j)})\}_{j \in \mathcal{J}}$. Using this data synthesis strategy, a dataset of size $|\mathcal{J}| = 22,000$ was generated for a prosumer cluster of size $|\mathcal{I}| = 100$, resulting in 2.2×10^6 individual HEMS simulations. The dataset \mathcal{D} is exchangeable, as each scenario depends only on its own inputs, and is used exclusively to train and validate the proposed ML surrogate model $\Phi_{1-\alpha}(\cdot)$ following the training procedure described in Section 4.2.

To evaluate the aggregator business model under the revenue-sharing incentive design defined in Eqs. (10a) and (10b), an additional set of 100 input scenarios was generated using the same data collection and sampling strategy described in Appendix A, and the same set of prosumers with photovoltaic and battery parameters consistent with those used in dataset \mathcal{D} . Unlike \mathcal{D} , where incentive prices were generated using a randomly sampled time-varying incentive factor multiplied by the up-regulation market price, the incentive price in this evaluation was defined using a fixed and time-invariant incentive factor such that $\lambda_t^{I,u} = \beta \lambda_t^U$ for all $t \in \mathcal{T}$, with $\beta \in \mathcal{S}_\beta = \{0.1, 0.2, \dots, 0.9\}$. Each scenario was used to solve the HEMS optimisation problem and subsequently aggregated in the same manner as before to construct a family of datasets \mathcal{D}_β of size 100, for all $\beta \in \mathcal{S}_\beta$. These datasets are used exclusively to evaluate the economic performance of each UQ method to support bidding decisions under uncertainty. The complete datasets used in this study are available at [40].

4.2. $\Phi_{1-\alpha}(\cdot)$ training

The ML model $\Phi_{1-\alpha}(\cdot)$ is trained on dataset \mathcal{D} following the procedure outlined in Algorithm 1. The dataset is partitioned into a training set $\mathcal{D}_{\text{train}}$ (10,000 samples), a

calibration set \mathcal{D}_{cal} (2,000 samples), and a test set $\mathcal{D}_{\text{test}}$ (10,000 samples). A relatively large test set is employed to ensure a low-variance and statistically reliable evaluation of coverage performance. The training set fits an NN with dropout layers $f_{\mathbf{y}}(\Theta)$; the calibration set applies CP to calibrate the prediction intervals derived by MCD using the conformity scores described in Section 3.2, ensuring coverage $1 - \alpha$; and the test set evaluates model performance.

To accelerate training, min–max normalisation is applied to obtain \mathcal{D}' and its subsets $\mathcal{D}'_{\text{train}}$, $\mathcal{D}'_{\text{cal}}$, and $\mathcal{D}'_{\text{test}}$. All inputs are min–max scaled except for the aggregated discharge power $b^{\text{dis,agg}}$ and energy capacity $b^{\text{cap,agg}}$, which are scaled by $b^{\text{dis,agg}}$ to ensure physical consistency. Consequently, $b^{\text{dis,agg}}$ is excluded from the final input features, as its effect is already embedded in the scaling. The normalised dataset therefore contains $6T + 1$ input features and T output features. Although recent market regulations have reduced the market time unit from one hour to 15 minutes, the publicly available datasets used in this study are provided at hourly resolution. Accordingly, the market time unit is assumed to be one hour, and the scheduling horizon is set to $T = 24$.

The NN $f_{\mathbf{y}}(\cdot)$ is trained on $\mathcal{D}'_{\text{train}}$ and validated using an 80:20 split. Hyperparameter tuning is conducted with the Optuna framework [41] over 100 optimisation trials, identifying the optimal configuration (layer depth, neurons, dropout rates, learning rates, and activations) that minimises validation loss. The final network is then trained using the selected parameters. Dropout governs the level of uncertainty captured in the MCD technique. Concrete dropout [42], which automatically learns dropout rates, was also tested but yielded a lower predictive accuracy compared to the Optuna-tuned regular dropout model. Thus, the regular dropout-based model is used to report the results.

Table 1: Neural network training hyperparameters

| Hyperparameter | Value |
|----------------------------------|-------------------------|
| Batch size | 32 |
| Number of epochs | 1000 |
| Optimiser | Adam |
| Learning rate | 3×10^{-4} |
| Loss metric | mean square error (MSE) |
| Network architecture | 2 hidden layers |
| Neurons per hidden layer | 256 |
| Hidden layer activation function | PRelu |
| Output activation function | Linear |
| Dropout probability (Layer 1) | 0.22 |
| Dropout probability (Layer 2) | 0.16 |

The trained model achieved a validation mean absolute error (MAE) of 2.79% relative to the aggregated discharge power (≈ 20 kW). As shown in Fig. 5(a), the residuals are symmetrically distributed around zero within ± 20 kW, while the root mean square error (RMSE) is 3.93% (≈ 30 kW) as shown in Fig. 5(b). These results confirm the robust predictive performance of the model. These metrics were calculated without applying MCD at the test time. The CP method operates on the min–max normalised dataset $\mathcal{D}'_{\text{cal}}$, ensuring that differing output scales do not distort conformity scores. The resulting normalised up-regulation flexibility intervals are clipped to $[0, 1]$, ensuring physical feasibility relative to the battery discharge limits. After calibration, two components are

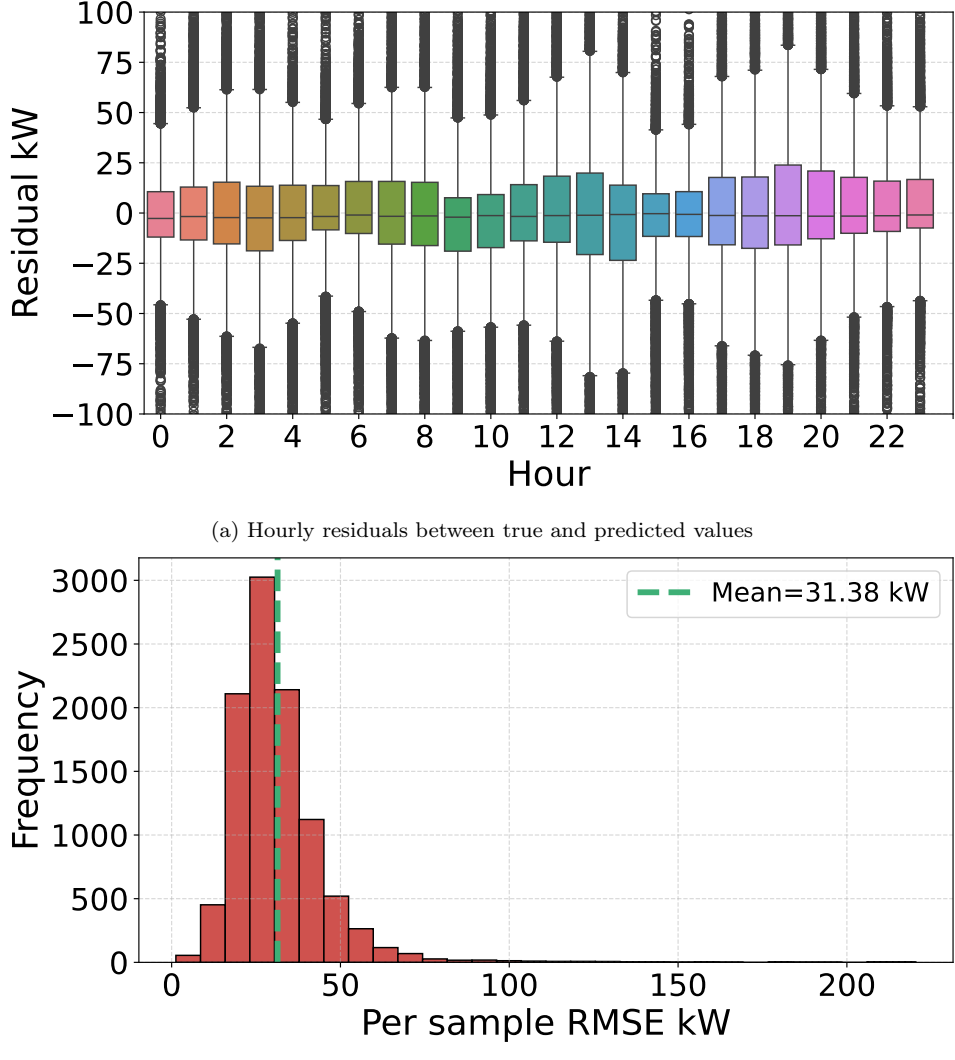


Figure 5: Error metrics for the NN trained with hyperparameters in Table 1

obtained: the dropout-based NN $f_y(\Theta)$ and the conformal calibration distance(s) \hat{q} , used to construct the final prediction interval ξ as in Steps 8–9 of Algorithm 1.

Finally, the trained prediction algorithm $\Phi_{1-\alpha}(\Theta)$ maps contextual inputs Θ , including load, solar generation, battery parameters, and market forecasts, to a prediction region ξ for aggregated up-regulation flexibility \mathbf{y} . This region guarantees a marginal coverage of at least $1 - \alpha$; $\Phi_{1-\alpha}(\Theta) = \xi$ such that $\mathbb{P}[\mathbf{y} \in \xi] \geq 1 - \alpha$. This calibrated prediction region is subsequently incorporated into the aggregator’s bidding strategy.

5. Results and discussion

5.1. UQ performance

This section evaluates the trained probabilistic prediction model $\Phi_{1-\alpha}$ based on the discussion in Section 4. The test set $(\Theta^{(j)}, \mathbf{y}^{(j)}) \in \mathcal{D}_{\text{test}}$ of size 10,000, is used to obtain prediction intervals $\xi^{(j)}$ with upper and lower bounds $\mathbf{u}^{(j)}$ and $\mathbf{l}^{(j)}$. Three baseline UQ methods based on NN with MCD outputs $\mathbf{Y}^{(j)}$ are considered for comparison:

1. **Sample mean** $\mu^{(j)}$ from Eq. (7a), used as a point estimate. Although interval metrics do not apply, the overbid frequency (Eq. (B.9)) can still be evaluated.
2. **Individual quantiles** $[\mathcal{Q}_t(\mathbf{Y}^{(j)}, \alpha), \mathcal{Q}_t(\mathbf{Y}^{(j)}, 1 - \alpha)]$, computed independently per hour $t \in \mathcal{T}$, ignoring temporal dependence.
3. **Naïve joint quantiles** $[\mathcal{Q}_t(\mathbf{Y}^{(j)}, \frac{\alpha}{T}), \mathcal{Q}_t(\mathbf{Y}^{(j)}, 1 - \frac{\alpha}{T})]$, applying a Bonferroni correction as a simplified joint constraint [43].

All methods adopt the P90 reliability target, corresponding to $\alpha = 0.10$, ensuring flexibility availability in at least 90% of the cases. For percentile-based methods, this implies an expected joint coverage of 80%. Each model uses $\mathcal{S} = 1000$ MCD samples from $\mathcal{D}_{\text{test}}$ to generate prediction intervals. These methods are evaluated using standard prediction interval metrics such as prediction interval coverage probability (PICP), which measures empirical coverage; mean prediction interval width (MPIW), which reflects the average width of the prediction intervals; and interval score (IS), which penalises both wide intervals and coverage violations. In addition, the frequency of the overbid metric from [8] quantifies the probability of reserve overestimation, which must remain below 10% to satisfy the P90 compliance criterion. The mathematical definitions of these prediction interval evaluation metrics are presented in Appendix B.

Table 2: Joint prediction interval quality comparison across various methods

| UQ Method | Expected Coverage | Joint PICP | Joint MPIW kW | Joint IS kW |
|-----------------------|-------------------|------------|---------------|-------------|
| Individual quantiles | 0.80 | 0.00 | 33.20 | 128.26 |
| Naïve joint quantiles | 0.80 | 0.00 | 86.56 | 122.58 |
| MCP | 0.80 | 0.80 | 163.90 | 167.86 |
| MMCP | 0.90 | 0.90 | 211.37 | 213.54 |
| PCP | 0.90 | 1.00 | 385.87 | 386.02 |
| CCP | 0.90 | 0.91 | 311.73 | 316.56 |

Table 2 shows that CP-based methods meet their intended coverage, while the non-CP baselines show near-zero joint PICP, reflecting overconfident intervals. For the CP methods, the joint IS aligns closely with MPIW, confirming the proper calibration. Conservativeness decreases in the order PCP, CCP, MMCP, and MCP, offering different reliability–interval width trade-offs. Ensuring that the lower bound meets the P90 requirement is crucial, as Energinet requires this criterion for valid bids. The frequency of daily overbids for each method is shown in Fig. 6. Benchmark methods fail to meet the 10% miscoverage limit, with MCD-based mean predictions showing nearly 100% violation. In contrast, MMCP, CCP, and PCP satisfy the requirement, while MCP slightly exceeds it (by about 1%). Among these, PCP produces the lowest miscoverage (0.14%), confirming its strong reliability. The slight shortfall of MCP can be remedied by conservative recalibration (e.g., setting $\alpha = 0.05$), which restores exact statistical validity at the cost of wider prediction intervals and reduced estimated flexibility, thereby potentially lowering aggregator revenue.

To meet the target P90, the CP methods widen their prediction intervals, lowering the flexibility estimate used for bidding. Figure 7 presents the distribution of daily average lower bounds as a fraction of the aggregated discharge capacity $b^{\text{dis,agg}}$. The PCP is the most conservative, while the NN sample mean remains closest to the true flexibility, but

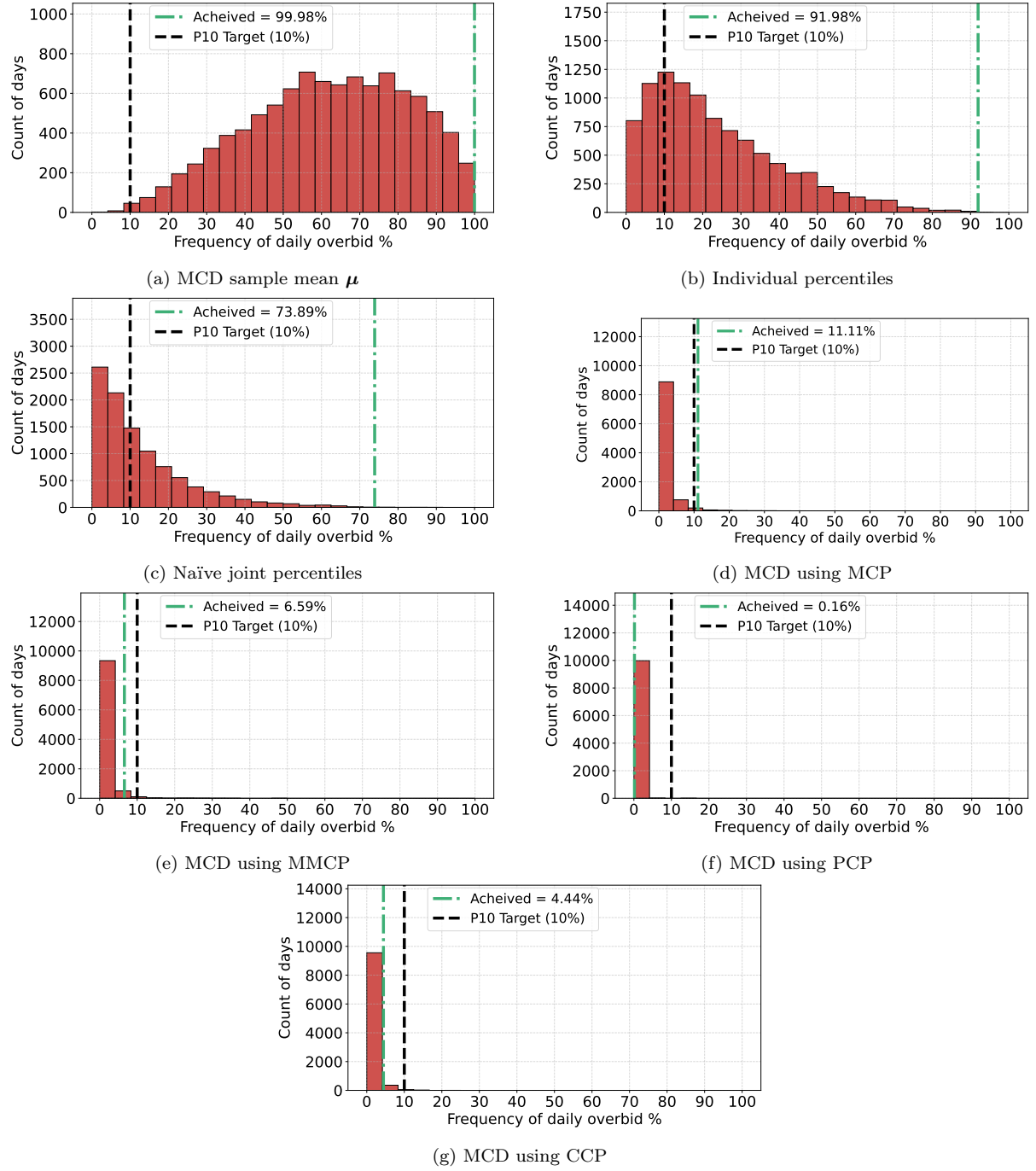


Figure 6: Histogram showing frequency of daily overbid for the implemented UQ methods

fails to control miscoverage. MMCP and MCP balance both aspects—achieving lower bounds at roughly 65% and 75% of the true value, respectively. Conversely, CCP and PCP predict 55% and 45%, offering high reliability at the cost of market competitiveness.

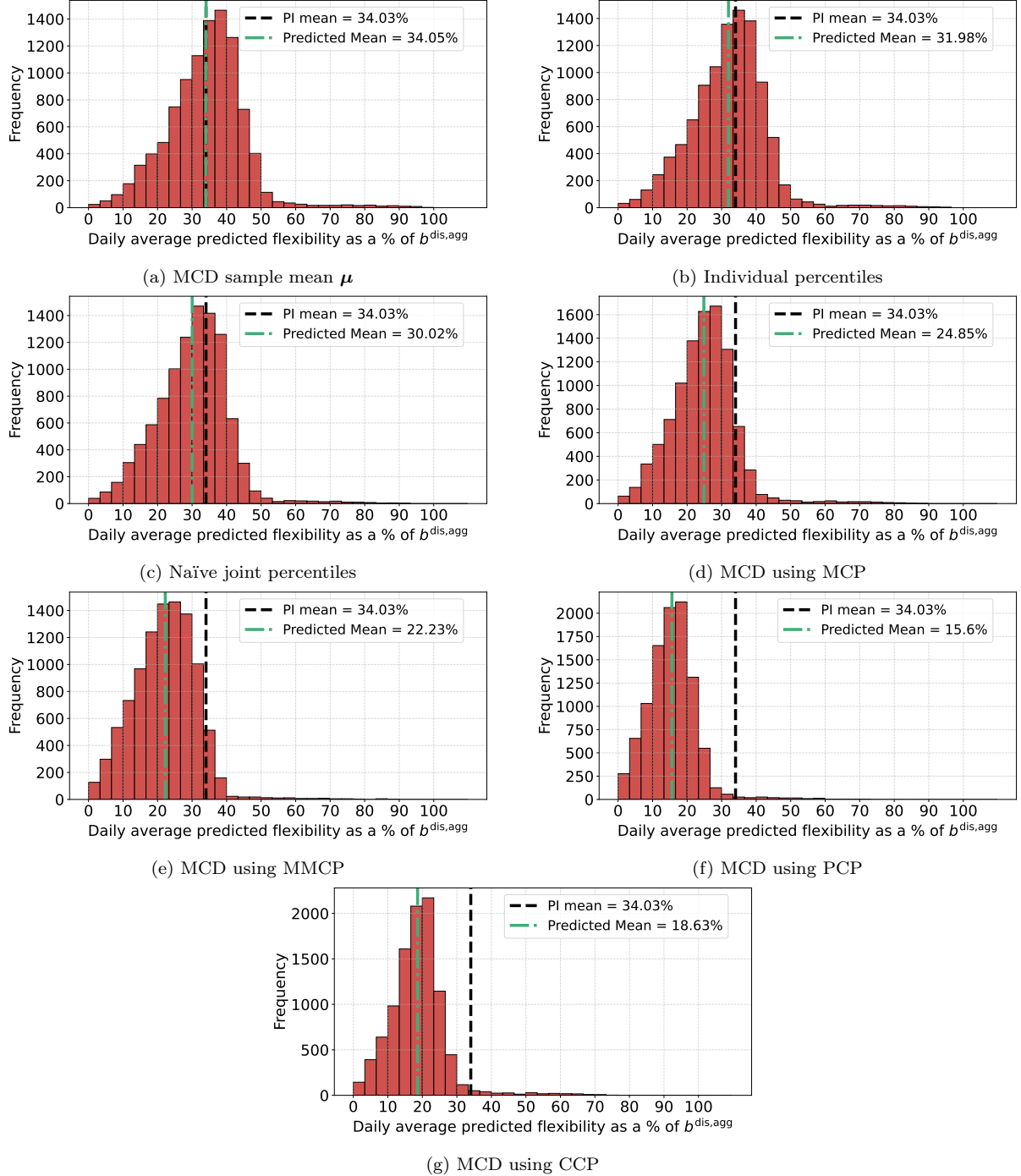


Figure 7: Histogram showing daily average predicted up-regulation flexibility lower bound as a % of aggregated maximum battery discharge power for the implemented UQ methods

Figure 8 further analyses the hourly variability in the width of the intervals and the lower-bound estimates. Due to Denmark’s low solar capacity factor ($\approx 12\%$) [44], residential batteries play a key role in providing flexible capacity in Watts’ HEMS algorithm. The mean prediction interval width (MPIW) peaks between 08:00–13:00 and 17:00–19:00, coinciding with higher demand and solar uncertainty. The CCP exhibits the greatest

variability, expected due to its adaptive calibration. The hourly lower-bound heatmaps (Fig. 8b) indicate that maximum flexibility occurs between 11:00–17:00, when batteries are typically charged and available for up-regulation. This aligns with the operational behaviour in residential HEMS systems. While PCP and CCP yield conservative bounds, MMCP and MCP provide a practical balance between reliability and usable flexibility, making them well-suited for market bidding.

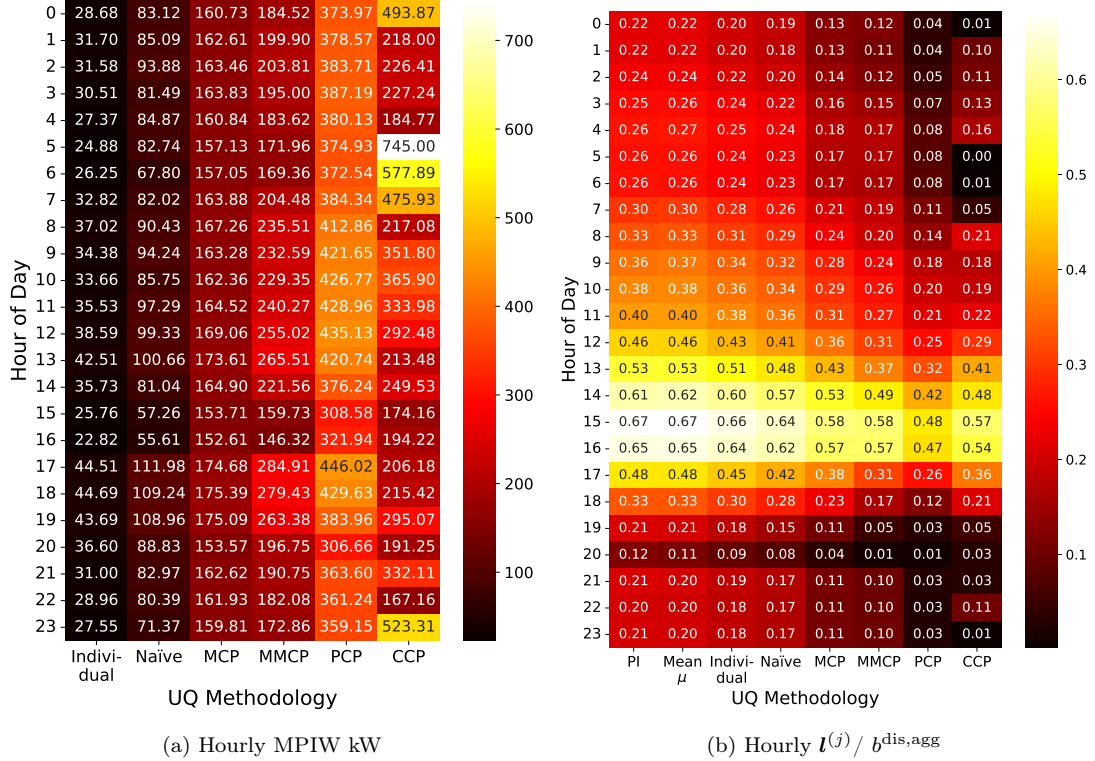


Figure 8: Hourly heatmap for different parameters across implemented UQ models

5.2. Aggregator business model performance

This section evaluates the aggregator’s bidding problem formulated in Eqs. (10a) and (10b), using the previously trained, calibrated, and validated UQ methods presented in Section 5.1. While Section 5.1 focused on predictive reliability, this section examines economic performance—specifically, how UQ methods influence bid robustness and profit margins under uncertainty. These analyses are performed using the dataset \mathcal{D}_β .

$$\gamma = \frac{\text{No. of hourly overbids in a day}}{\text{Total number of bids in a day}} = \frac{\sum_{t \in \mathcal{T}} \mathbb{1}(y_t^{(j)} < x_t^u \mid x_t^u > 0)}{\sum_{t \in \mathcal{T}} \mathbb{1}(x_t^u > 0)} \quad (11)$$

Energinet imposes penalties for overbidding as per Section 2.2.1 of its FCAS tender conditions [29], which state that payments are reduced proportionally for hours of non-delivery or non-availability. These penalties apply separately to capacity and activation markets and directly impact realised profit. Interpreting this clause, if 6 of 24 contracted hours are unavailable, 25% of the payment is forfeited. However, “contract period” may refer to individual hours or to the entire daily auction period. Hence, adjusted profits are

reported under both interpretations. Equation (11) defines the conditional daily overbid frequency, quantifying the share of hours where overbidding occurs among all hours with bids ($x_t^u > 0$). This term acts as a penalty factor when the contract period is interpreted as all hourly bids placed within a day.

$$R(\mathbf{x}^u, \beta) = [1 - \beta] \sum_{t \in \mathcal{T}} \lambda_t^U x_t^u \quad (12a)$$

$$R_1(\mathbf{x}^u, \beta) = \sum_{t \in \mathcal{T}} \mathbb{1}(x_t^u \leq y_t^{(j)}) \lambda_t^U x_t^u - \beta \sum_{t \in \mathcal{T}} \lambda_t^U x_t^u \quad (12b)$$

$$R_2(\mathbf{x}^u, \beta) = [1 - \gamma - \beta] \sum_{t \in \mathcal{T}} \lambda_t^U x_t^u \quad (12c)$$

The unadjusted (baseline) profit is defined in Eq. (12a). Equation (12b) defines the hourly profit, where each hour is settled independently; non-delivery forfeits that hour’s revenue. Equation (12c) models daily settlement, penalising full-day revenue by γ , the fraction of overbid hours. In both, incentives are paid fully to prosumers, proportional to their capacity share, regardless of aggregator-level unavailability.

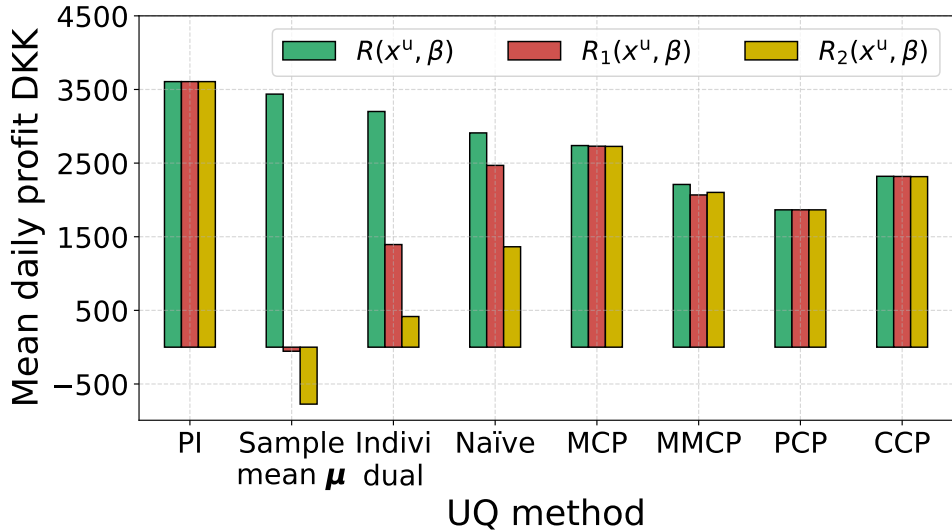


Figure 9: Mean daily unadjusted and adjusted profit for all UQ methods across all $\beta \in \mathcal{S}_\beta$

Figure 9 compares unadjusted and adjusted daily profits for all UQ methods against β values. The perfect-information (PI) benchmark indicates the maximum daily profit achievable under PI. Bidding with the sample mean μ or individual quantiles yields the highest unadjusted profits, but suffers severe losses once penalties are applied, especially under the daily scheme, where the sample mean leads to net losses. Persistent overbidding also violates P90 reliability and risks market suspension. Conversely, CP-based methods demonstrate superior robustness. Both MCP and MMCP achieve the highest adjusted profits, while PCP and CCP, though more conservative, outperform all non-CP baselines under penalisation. Integrating CP with NN-based MCD thus provides both reliability and profitability.

Table 3 quantifies the mean profit of each method relative to the PI benchmark. The sample mean and individual quantile methods initially match or exceed PI profit due to overbidding, but experience drastic reductions once penalties are applied. In contrast, CP-based methods maintain stable performance, with MCP consistently yielding

Table 3: Mean percentage of PI profit for each UQ method

| UQ Method | Mean percentage of PI profit (%) | | |
|-----------------------|----------------------------------|----------------------------|----------------------------|
| | $R(\mathbf{x}^u, \beta)$ | $R_1(\mathbf{x}^u, \beta)$ | $R_2(\mathbf{x}^u, \beta)$ |
| Sample mean μ | 101 | -56 | -97 |
| Individual quantiles | 94 | 10 | -43 |
| Naïve joint quantiles | 87 | 46 | -10 |
| MCP | 71 | 69 | 68 |
| MMCP | 61 | 61 | 61 |
| PCP | 43 | 43 | 43 |
| CCP | 52 | 52 | 52 |

the highest adjusted profit and MMCP showing uniform behaviour across both penalty schemes. Although PCP and CCP are more conservative, they preserve a higher share of PI profit after adjustment compared to the overbidding-prone benchmarks. This highlights the trade-off between aggressive bidding and delivery reliability, underscoring the practical value of conformal approaches in ensuring sustainable profits under uncertainty. Achieving such reliability typically reduces the best-case profit by 30–60%, depending on the conservativeness of the chosen CP method. While this also lowers prosumer payments (as incentives are proportional to submitted bids), it preserves residual flexibility that could later be monetised in the intraday or activation markets.

Figure 10 presents the sensitivity of aggregator performance to the revenue-sharing parameter β . Figures 10(a) and (b) show that CP-based methods consistently outperform benchmark approaches in terms of adjusted profit across all values of β . As expected, adjusted profit decreases monotonically as the prosumer incentive increases. This behaviour arises because the bid volume (Fig. 10(c)) exhibits only a weak response to increasing β , with an estimated supply elasticity ϵ_s in the range of 3–5%. Consequently, the current HEMS algorithm assigns a low marginal value to additional incentives, offering most of the available flexibility even at relatively small incentive levels. This observation is further supported by the fact that, across 100 scenarios, the optimal incentive factor was $\beta^* = 0.1$ in 97 cases and $\beta^* = 0.2$ in the remaining three cases, indicating that allocating only 10–20% of market revenue to prosumers typically maximises aggregator profit. This outcome is likely driven by the relatively high retail electricity purchase prices faced by prosumers compared to aggregation incentives, making it economically rational for prosumers to offer nearly their full available flexibility regardless of the incentive level. These results indicate a potential prosumer engagement barrier associated with the low marginal gains from participating in flexibility aggregation. This may reduce incentives for active prosumer involvement. The findings suggest that complementary policy or market design measures could be considered to support and potentially enhance prosumer engagement. Such measures may include electricity price tax adjustments, grid tariff subsidies, or modest fixed participation incentives.

6. Conclusions and future scope

This study investigated uncertainty-aware flexibility forecasting for aggregators participating in European ancillary service markets under regulatory reliability constraints. A hybrid uncertainty quantification framework combining Monte Carlo dropout (MCD) with conformal prediction (CP) was developed and embedded within an aggregator bidding model to address the substantial epistemic uncertainty arising from limited behavioural data and reliance on exogenous forecasts. Using a large-scale synthetic dataset

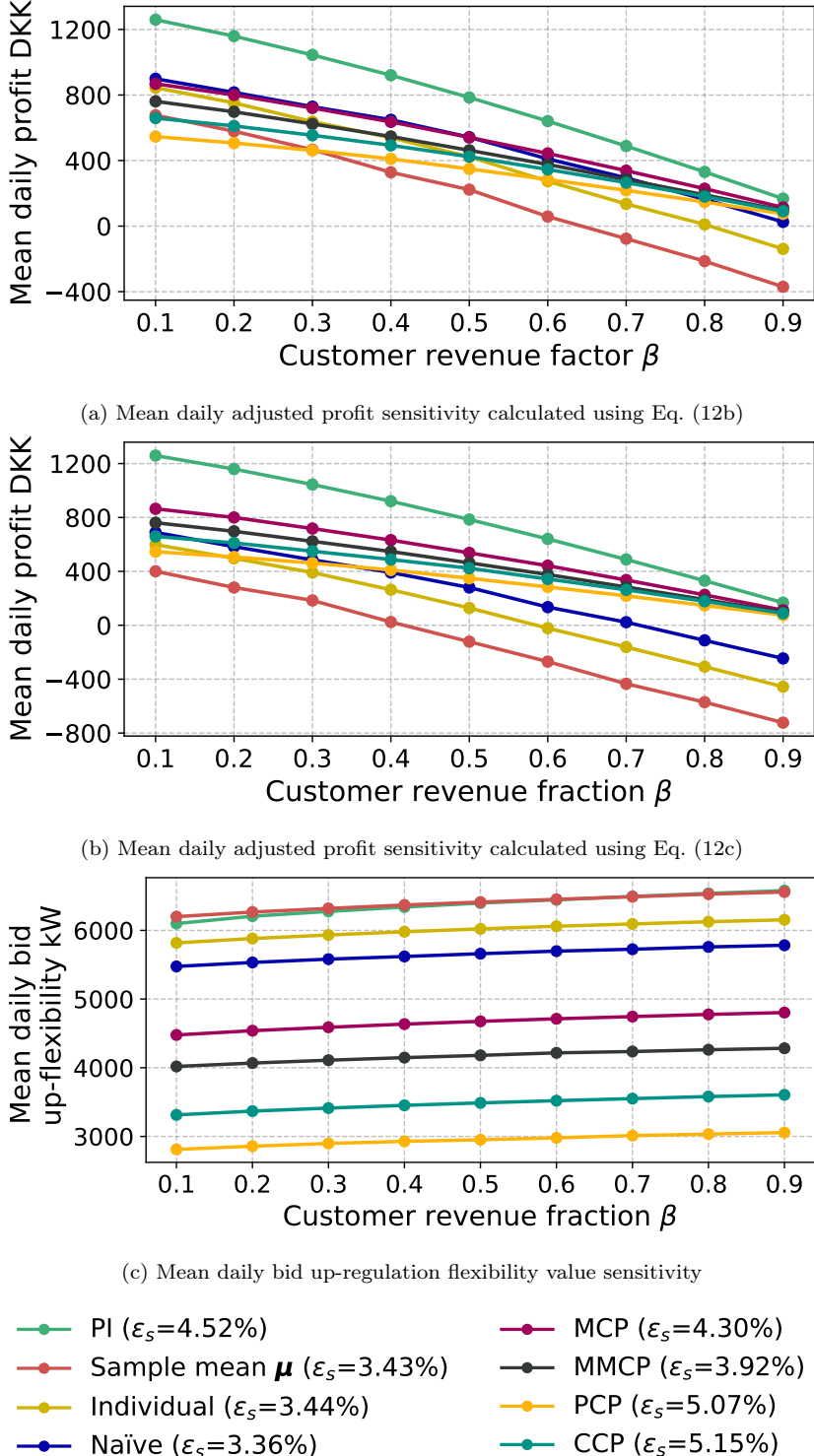


Figure 10: Revenue factor β sensitivity analysis

generated from an industry-grade home energy management system, the proposed approach was evaluated in terms of both P90 compliance and economic performance.

The results show that the hybrid MCD-CP-based methods deliver well-calibrated prediction intervals and effectively control overbidding risk in capacity markets. Compared to uncalibrated MCD benchmarks, the hybrid MCD-CP framework satisfies the P90 reliability requirement while retaining a substantial share of the PI profit, achieving up to approximately 70% in the Danish FCAS capacity market. From an economic perspective, the analysis further indicates that aggregator profit decreases monotonically with increasing prosumer incentives due to weak flexibility supply elasticity (3–5%), implying that prosumers offer most of their available flexibility even at low incentive levels. This results in low marginal gains from higher compensation and suggests a potential prosumer engagement barrier under current market designs, highlighting the possible need for complementary policy or market design measures in settings characterised by thin aggregator profit margins.

While the proposed framework is computationally efficient and market-compliant, the analysis is subject to several limitations. The revenue-sharing-based incentive design relies on accurate market price forecasts, which may not be available in practice and therefore warrants further investigation. In addition, the use of a centralised ML training framework may raise data privacy and security concerns for prosumers. Future work may include: (i) systematic evaluation of the framework under epistemic uncertainty, such as forecast errors and training dataset size sensitivity; (ii) adaptation to decentralised learning paradigms, including federated learning; (iii) development of incentive mechanisms that explicitly account for market price uncertainty; and (iv) strategies for reallocating residual flexibility arising from conservative day-ahead bidding to markets operating closer to real time. These extensions could further enhance the robustness and practical applicability of uncertainty-aware aggregator bidding strategies.

CRediT authorship contribution statement

Yogesh Pipada Sunil Kumar: Conceptualisation, Methodology, Software, Formal analysis, Investigation, Writing - original draft, Writing - review and editing. **S. Ali Pourmousavi:** Conceptualisation, Supervision, Project administration, Funding acquisition, Writing - review and editing. **Jon A.R. Liisberg:** Supervision, Writing - review and editing. **Julian Lesmos-Vinasco:** Supervision, Writing - review and editing.

Acknowledgement

This project is supported by the Australian Government Research Training Program (RTP) through the University of Adelaide, and a supplementary scholarship provided by Watts A/S, Denmark. During the preparation of this work, the authors used ChatGPT [45] in order to improve readability and language. After using this tool, the authors reviewed and edited the content as needed and take full responsibility for the content of the publication.

References

- [1] A. Attarha, P. Scott, J. Iria, S. Thiebaux, Network-Secure and Price-Elastic Aggregator Bidding in Energy and Reserve Markets, *IEEE Transactions on Smart Grid* 12 (3) (2021) 2284–2294. doi:10.1109/TSG.2021.3049464.

[2] European Parliament and Council of the European Union, Directive (EU) 2019/944 on common rules for the internal market for electricity (recast), Official Journal of the European Union, L 158, 14 June 2019, pp. 125–199, accessed: 2025-08-15 (2019). URL <https://eur-lex.europa.eu/eli/dir/2019/944/oj/eng>

[3] European Parliament and Council of the European Union, Regulation (EU) 2024/1747 amending regulations (EU) 2019/942 and (EU) 2019/943 on improving the union's electricity market design, Official Journal of the European Union, L 2024/1747, 26 June 2024, accessed: 2025-08-15 (2024). URL https://eur-lex.europa.eu/legal-content/EN/TXT/?uri=OJ:L_202401747

[4] European Commission, Targeted Consultation to Support the Establishment of a New Network Code on Demand Response, accessed: 2025-08-13 (2025). URL https://energy.ec.europa.eu/consultations/targeted-consultation-support-establishment-new-network-code-demand-response_en

[5] D. Watari, I. Taniguchi, T. Onoye, Duck Curve Aware Dynamic Pricing and Battery Scheduling Strategy Using Reinforcement Learning, *IEEE Transactions on Smart Grid* 15 (1) (2024) 457–471. doi:10.1109/TSG.2023.3288355.

[6] N. T. Dinh, S. Karimi-Arpanahi, R. Yuan, S. A. Pourmousavi, M. Guo, J. A. R. Liisberg, J. Lemos-Vinasco, Modeling Irrational Behavior of Residential End Users Using Non-Stationary Gaussian Processes, *IEEE Transactions on Smart Grid* 15 (5) (2024) 4636–4648. doi:10.1109/TSG.2024.3382771.

[7] M. Massaoudi, K. R. Davis, K. Akramul Haque, Analysis and Quantification of Demand Flexibility for Resilient Distribution Networks: A Systematic Review, *IEEE Access* 13 (2025) 42650–42668. doi:10.1109/ACCESS.2025.3548526.

[8] G. A. Lunde, E. V. Damm, P. A. Gade, J. Kazempour, Aggregator of Electric Vehicles Bidding in Nordic FCR-D Markets: A Chance-Constrained Program, *IEEE Transactions on Power Systems* (2025) 1–12doi:10.1109/TPWRS.2025.3558868.

[9] P. Boopathy, M. Liyanage, N. Deepa, M. Velavali, S. Reddy, P. K. R. Maddikunta, N. Khare, T. R. Gadekallu, W.-J. Hwang, Q.-V. Pham, Deep learning for intelligent demand response and smart grids: A comprehensive survey, *Computer Science Review* 51 (2024) 100617. doi:<https://doi.org/10.1016/j.cosrev.2024.100617>. URL <https://www.sciencedirect.com/science/article/pii/S1574013724000017>

[10] M. Sun, T. Zhang, Y. Wang, G. Strbac, C. Kang, Using Bayesian Deep Learning to Capture Uncertainty for Residential Net Load Forecasting, *IEEE Transactions on Power Systems* 35 (1) (2020) 188–201. doi:10.1109/TPWRS.2019.2924294.

[11] Y. Yang, W. Li, T. A. Gulliver, S. Li, Bayesian Deep Learning-Based Probabilistic Load Forecasting in Smart Grids, *IEEE Transactions on Industrial Informatics* 16 (7) (2020) 4703–4713. doi:10.1109/TII.2019.2942353.

[12] N. Bassamzadeh, R. Ghanem, Multiscale stochastic prediction of electricity demand in smart grids using Bayesian networks, *Applied Energy* 193 (2017) 369–380.

doi:<https://doi.org/10.1016/j.apenergy.2017.01.017>.
URL <https://www.sciencedirect.com/science/article/pii/S0306261917300193>

- [13] Z. Ding, Q. Lu, X. Wei, Z. Xu, X. Li, S. Guo, C. Gong, Y. Hu, Y. Han, Forecasting Flexible Regulation Capabilities of Electric Vehicles: A Probabilistic Approach With Bayesian Neural Networks and Transformer, *IEEE Transactions on Industry Applications* 61 (4) (2025) 5468–5478. doi:[10.1109/TIA.2025.3548578](https://doi.org/10.1109/TIA.2025.3548578).
- [14] M. Baragatti, C. Céline, B. Cloez, D. Métivier, I. Sanchez, Approximate Bayesian Computation with Deep Learning and Conformal prediction (2025). arXiv:2406.04874.
URL <https://arxiv.org/abs/2406.04874>
- [15] Y. Gal, Z. Ghahramani, Dropout as a Bayesian approximation: Representing model uncertainty in deep learning, in: M. F. Balcan, K. Q. Weinberger (Eds.), *Proceedings of the 33rd International Conference on Machine Learning*, Vol. 48 of *Proceedings of Machine Learning Research*, PMLR, New York, New York, USA, 2016, pp. 1050–1059.
URL <https://proceedings.mlr.press/v48/gal16.html>
- [16] B. Lambert, F. Forbes, S. Doyle, H. Dehaene, M. Dojat, Trustworthy clinical AI solutions: A unified review of uncertainty quantification in Deep Learning models for medical image analysis, *Artificial Intelligence in Medicine* 150 (2024) 102830. doi:<https://doi.org/10.1016/j.artmed.2024.102830>.
URL <https://www.sciencedirect.com/science/article/pii/S0933365724000721>
- [17] R. Zhao, K. Wang, Y. Xiao, F. Gao, Z. Gao, Leveraging Monte Carlo Dropout for Uncertainty Quantification in Real-Time Object Detection of Autonomous Vehicles, *IEEE Access* 12 (2024) 33384–33399. doi:[10.1109/ACCESS.2024.3355199](https://doi.org/10.1109/ACCESS.2024.3355199).
- [18] M. Bhih, Z. E. Abou Elassad, M. Ameksa, A. El Boustani, O. El Meslouhi, D. E. Abou Elassad, Quantifying Uncertainty in Energy Demand Forecasts: A Probabilistic Modeling Approach, in: 2025 5th International Conference on Innovative Research in Applied Science, Engineering and Technology (IRASET), 2025, pp. 1–4. doi:[10.1109/IRASET64571.2025.11008242](https://doi.org/10.1109/IRASET64571.2025.11008242).
- [19] L. L. Folgoc, V. Baltatzis, S. Desai, A. Devaraj, S. Ellis, O. E. M. Manzanera, A. Nair, H. Qiu, J. Schnabel, B. Glocker, Is MC Dropout Bayesian? (2021). arXiv:2110.04286.
URL <https://arxiv.org/abs/2110.04286>
- [20] K. Shridhar, F. Laumann, M. Liwicki, A Comprehensive guide to Bayesian Convolutional Neural Network with Variational Inference (2019). arXiv:1901.02731.
URL <https://arxiv.org/abs/1901.02731>
- [21] Y.-C. Huang, J. Padarian, B. Minasny, A. B. McBratney, Using Monte Carlo conformal prediction to evaluate the uncertainty of deep-learning soil spectral models, *SOIL* 11 (2) (2025) 553–563. doi:[10.5194/soil-11-553-2025](https://doi.org/10.5194/soil-11-553-2025).
URL <https://soil.copernicus.org/articles/11/553/2025/>

- [22] G. Shafer, V. Vovk, A tutorial on conformal prediction (2007). [arXiv:0706.3188](https://arxiv.org/abs/0706.3188).
URL <https://arxiv.org/abs/0706.3188>
- [23] A. N. Angelopoulos, R. F. Barber, S. Bates, Theoretical Foundations of Conformal Prediction (2025). [arXiv:2411.11824](https://arxiv.org/abs/2411.11824).
URL <https://arxiv.org/abs/2411.11824>
- [24] C. O'Connor, M. Bahloul, R. Rossi, S. Prestwich, A. Visentin, Conformal Prediction for electricity price forecasting in the day-ahead and real-time balancing market, *Energy and AI* 21 (2025) 100571. doi: <https://doi.org/10.1016/j.egyai.2025.100571>.
URL <https://www.sciencedirect.com/science/article/pii/S266654682500103X>
- [25] Y. Renkema, N. Brinkel, T. Alskai, Conformal prediction for stochastic decision-making of PV power in electricity markets, *Electric Power Systems Research* 234 (2024) 110750. doi: <https://doi.org/10.1016/j.epsr.2024.110750>.
URL <https://www.sciencedirect.com/science/article/pii/S0378779624006369>
- [26] R. Rossellini, R. Foygel Barber, R. Willett, Integrating Uncertainty Awareness into Conformalized Quantile Regression, in: S. Dasgupta, S. Mandt, Y. Li (Eds.), *Proceedings of The 27th International Conference on Artificial Intelligence and Statistics*, Vol. 238 of *Proceedings of Machine Learning Research*, PMLR, 2024, pp. 1540–1548.
URL <https://proceedings.mlr.press/v238/rossellini24a.html>
- [27] V. Dheur, M. Fontana, Y. Estievenart, N. Desobry, S. B. Taieb, A Unified Comparative Study with Generalized Conformity Scores for Multi-Output Conformal Regression (2025). [arXiv:2501.10533](https://arxiv.org/abs/2501.10533).
URL <https://arxiv.org/abs/2501.10533>
- [28] W. A/S, Watts – Intelligent styring af vedvarende energi, <https://www.watts.dk/>, accessed: 2025-09-24 (2025).
- [29] Energinet, Ancillary Services to Be Delivered in Denmark – Tender Conditions, https://en.energinet.dk/media/uuzfldlp/21_10162-21-ancillary-services-to-be-delivered-in-denmark-tender-conditions-10527603_1_1.pdf, accessed: 2025-05-01.
- [30] Energinet, Prequalification of Units and Aggregated Portfolios, <https://energinet.dk/media/ox0gqmvw/gaeldende-prequalification-of-units-and-aggregated-portfolios.pdf>, accessed: 2025-05-01.
- [31] R. Rossellini, R. F. Barber, R. Willett, Integrating Uncertainty Awareness into Conformalized Quantile Regression (2024). [arXiv:2306.08693](https://arxiv.org/abs/2306.08693).
URL <https://arxiv.org/abs/2306.08693>
- [32] Y. Zhou, L. Lindemann, M. Sesia, Conformalized Adaptive Forecasting of Heterogeneous Trajectories (2024). [arXiv:2402.09623](https://arxiv.org/abs/2402.09623).
URL <https://arxiv.org/abs/2402.09623>

- [33] M. Cocheteux, J. Moreau, F. Davoine, Uncertainty-Aware Online Extrinsic Calibration: A Conformal Prediction Approach, in: 2025 IEEE/CVF Winter Conference on Applications of Computer Vision (WACV), IEEE, 2025, p. 6167–6176. doi:10.1109/wacv61041.2025.00601.

URL <http://dx.doi.org/10.1109/WACV61041.2025.00601>
- [34] Z. Wang, R. Gao, M. Yin, M. Zhou, D. M. Blei, Probabilistic Conformal Prediction Using Conditional Random Samples (2022). arXiv:2206.06584.

URL <https://arxiv.org/abs/2206.06584>
- [35] S. Sun, R. Yu, Copula Conformal Prediction for Multi-step Time Series Forecasting (2024). arXiv:2212.03281.

URL <https://arxiv.org/abs/2212.03281>
- [36] S. H. Sun, R. Yu, CopulaCPTS: Code for Copula Conformal Prediction for Multi-step Time Series Forecasting, <https://github.com/Rose-STL-Lab/CopulaCPTS>, accessed: 2025-05-24 (2024).
- [37] J. L. Vinasco, Decision support tools for smart Home Energy Management Systems (HEMSs), Ph.D. thesis, Technical University of Denmark (2022).
- [38] Watts, Watts Homegrid, accessed: 2025-10-03 (2025).

URL <https://www.watts.dk/homegrid>
- [39] Energi Data Service, API guide, <https://www.energidataservice.dk/guides/api-guides>, accessed: 2025-05-01.
- [40] Y. Pipada, Synthetic data for aggregated prosumers, <https://github.com/YogeshPipada/Synthetic-data-for-aggregated-prosumers>, CC BY 4.0; dataset supporting “Calibrated uncertainty quantification for prosumer flexibility aggregation in ancillary service markets” (2025).
- [41] T. Akiba, S. Sano, T. Yanase, T. Ohta, M. Koyama, Optuna: A Next-generation Hyperparameter Optimization Framework, in: Proceedings of the 25th ACM SIGKDD International Conference on Knowledge Discovery and Data Mining, 2019.
- [42] Y. Gal, J. Hron, A. Kendall, Concrete Dropout (2017). arXiv:1705.07832.

URL <https://arxiv.org/abs/1705.07832>
- [43] K. Baker, A. Bernstein, Joint Chance Constraints in AC Optimal Power Flow: Improving Bounds Through Learning, IEEE Transactions on Smart Grid 10 (6) (2019) 6376–6385. doi:10.1109/TSG.2019.2903767.
- [44] Danish Energy Agency, The Danish Energy Agency launches improved LCoE calculator, <https://ens.dk/en/press/danish-energy-agency-launches-improved-lcoe-calculator>, accessed: 2025-06-12.
- [45] OpenAI, ChatGPT.

URL <https://openai.com/chatgpt>

[46] IEA PVPS Task 1 and Danish Energy Agency, National survey report of PV power applications in denmark - 2016, Tech. rep., International Energy Agency Photovoltaic Power Systems Programme (IEA PVPS), accessed: 2025-05-20 (2017).
 URL https://iea-pvps.org/wp-content/uploads/2020/01/National_Survey_Report_of_PV_Power_Applications_in_Denmark_-_2016.pdf

[47] IEA PVPS Task 1 and Danish Energy Agency, National survey report of PV power applications in denmark - 2017, Tech. rep., International Energy Agency Photovoltaic Power Systems Programme (IEA PVPS), accessed: 2025-05-20 (2018).
 URL https://iea-pvps.org/wp-content/uploads/2020/01/National_Survey_Report_of_PV_Power_Applications_in_Denmark_-_2017.pdf

[48] IEA PVPS Task 1 and Energinet, National survey report of PV power applications in denmark - 2018, Tech. rep., International Energy Agency Photovoltaic Power Systems Programme (IEA PVPS), accessed: 2025-05-20 (2019).
 URL https://iea-pvps.org/wp-content/uploads/2020/01/NSR_Denmark_2018.pdf

[49] M. Sandelic, A. Sangwongwanich, F. Blaabjerg, Robustness Evaluation of PV-Battery Sizing Principle Under Mission Profile Variations, in: 2020 IEEE Energy Conversion Congress and Exposition (ECCE), 2020, pp. 545–552. doi:10.1109/ECCE44975.2020.9235720.

[50] J. Moshövel, K.-P. Kairies, D. Magnor, M. Leuthold, M. Bost, S. Gährs, E. Szczechowicz, M. Cramer, D. U. Sauer, Analysis of the maximal possible grid relief from PV-peak-power impacts by using storage systems for increased self-consumption, *Applied Energy* 137 (2015) 567–575. doi:<https://doi.org/10.1016/j.apenergy.2014.07.021>.
 URL <https://www.sciencedirect.com/science/article/pii/S0306261914007028>

[51] BYD Company Ltd., BYD Battery-Box Premium HV-AU Datasheet V1.2, Tech. rep., BYD Company Ltd., accessed: 2025-05-20 (2020).
 URL https://bydbatterybox.com/uploads/downloads/BYD%20Battery-Box%20Premium_Datasheet_HV-AU%20V1.2%20EN-5eec6422498ad.pdf

[52] R. Yuan, S. A. Pourmousavi, W. L. Soong, A. J. Black, J. A. R. Liisberg, J. Lemos-Vinasco, A synthetic dataset of Danish residential electricity prosumers, *Scientific Data* 10 (1) (2023) 371. doi:10.1038/s41597-023-02271-3.
 URL <https://doi.org/10.1038/s41597-023-02271-3>

[53] S. Pfenninger, I. Staffell, *Renewables.ninja*, <https://www.renewables.ninja>, accessed: 2025-05-20 (2016).

[54] S. Pfenninger, I. Staffell, Long-term patterns of European PV output using 30 years of validated hourly reanalysis and satellite data, *Energy* 114 (2016) 1251–1265. doi:10.1016/j.energy.2016.08.060.
 URL <https://doi.org/10.1016/j.energy.2016.08.060>

[55] I. Staffell, S. Pfenninger, Using Bias-Corrected Reanalysis to Simulate Current and Future Wind Power Output, *Energy* 114 (2016) 1224–1239. doi:10.1016/j.energy.

2016.08.068.

URL <https://doi.org/10.1016/j.energy.2016.08.068>

- [56] Cerius A/S, Tariffer og netabonnement, accessed: 2025-05-20 (2025).
URL <https://cerius.dk/priser-og-tariffer/tariffer-og-netabonnement/>
- [57] Cerius A/S, Historiske tariffer og netabonnement, accessed: 2025-05-20 (2025).
URL <https://cerius.dk/priser-og-tariffer/tariffer-og-netabonnement/historiske-tariffer/>

Appendix A. Data collection and input scenario sampling strategy

This section details the data collection process and input scenario sampling strategy adopted in this study as part of the synthetic data generation framework illustrated in Fig. 4.

To construct the dataset for training, calibration and validation, we simulated the operation of the HEMS for $|\mathcal{I}|$ residential prosumers located in the DK1 region of Denmark. The size of the solar PV system of each prosumer was randomly sampled according to the distribution reported in the International Energy Agency's national survey reports from 2012–2018 [46, 47, 48]. The battery capacity for each household was estimated using a simplified sizing rule proposed in [49, 50], which sets the storage capacity to approximately 1.5 times the size of PV for Denmark. To introduce variability, the size multiplier was randomly selected from the range [1.2, 1.7]. To ensure that the resulting capacities are practically deployable, each estimated battery size was matched to the nearest available model of the BYD residential product line [51], adopting the corresponding nameplate capacity $b^{\text{cap},i}$, the rated discharge power $b^{\text{dis},i}$ and the round-trip efficiency of the product datasheet for each individual prosumer $i \in \mathcal{I}$.

The disaggregated load and solar generation data for each prosumer $i \in \mathcal{I}$ were required to simulate the HEMS algorithm. The load data, \mathbf{x}^l, i , were obtained from the synthetic dataset developed by the authors in [52], containing 100,000 daily consumption profiles with hourly resolution, categorised into workdays and non-workdays. Solar generation data was obtained from the Renewables.ninja platform [53], based on the methodology in [54, 55], which generates simulated hourly solar generation data for various PV configurations and regions. Data were generated for 5,100 daily solar profiles across seven distinct panel tilt angles ($25^\circ, 36^\circ, 40^\circ, 42^\circ, 47^\circ, 58^\circ, 69^\circ$) for a 1 kW PV system. Individual prosumer generation profiles, \mathbf{x}^s, i , were then derived by scaling these 1 kW profiles according to each prosumer's assigned PV capacity. Since the load and solar profiles were not temporally aligned, randomly paired daily load–solar profile combinations were created for each prosumer.

Electricity market data for Denmark were obtained using the Energinet Data Service API [39]. The prosumer electricity sale price profiles, $\boldsymbol{\lambda}^s$, were derived from day-ahead market (DAM) daily price data for the DK1 bidding zone, covering the period from January 2023 to January 2025. The corresponding purchase price profiles, $\boldsymbol{\lambda}^p$, were calculated by adding applicable grid tariffs and a 25% value-added tax (VAT) to the sale prices. The grid tariffs for the simulation period were obtained from one of the Denmark distribution system operators, Cerius [56, 57]. Similarly, market price profiles for mFRR up-regulation capacity, $\boldsymbol{\lambda}^u$, were extracted for the period August 2021 to January 2025. Binary activation signals for mFRR up-regulation, \mathbf{a}^\uparrow , were obtained for January 2021 to January 2025. To enhance data diversity, additional activation samples were synthetically

generated by modelling the tetrachoric correlation structure of the historical activation signal. Multiple scenarios of the up-regulation incentive, $\lambda^{I,u}$, were generated by scaling the historical mFRR up-regulation capacity prices with random multipliers independently drawn from a uniform distribution in $[0, 1]$ at each time interval, thus producing a wide range of incentive pricing scenarios. This scaling approach is consistent with the logical constraint that the incentive offered to prosumers must not exceed the market clearing price.

Because the various market datasets were not temporally aligned with the load and solar profiles, we generated combinations of randomly sampled market scenarios. Each scenario included a distinct set of daily values for electricity prices, up-regulation prices, and activation signals. To ensure consistency and allow aggregation at the cluster level, each market scenario was applied uniformly across all $|\mathcal{I}|$ prosumers, each with unique load, generation, and battery characteristics. This approach ensures a diverse yet coherent input dataset suitable for obtaining the aggregated behaviour of the prosumers under realistic market and operational variability.

Appendix B. Prediction interval evaluation metrics

To assess the quality of the prediction intervals generated by our probabilistic forecasting algorithm, we employ a set of established evaluation metrics. Let $(\Theta^{(j)}, y^{(j)})$ denote the j^{th} instance in the test dataset $\mathcal{D}_{\text{test}}$. Let $\xi^{(j)} = \Phi_{1-\alpha}(\Theta^{(j)})$ represent the corresponding prediction interval at a coverage level of $1 - \alpha$. The element-wise upper and lower bounds of this interval are denoted by $\mathbf{u}^{(j)} = \sup \xi^{(j)}$ and $\mathbf{l}^{(j)} = \inf \xi^{(j)}$, respectively. The resulting bounding hyperrectangle $\mathcal{B}_{\xi}^{(j)}$ is defined accordingly, as shown in Eq. (4), and serves as the basis for all interval-based evaluations in this case study.

This adjustment only affects the PCP-based predictions, leading to more conservative bounds, and does not affect the other methods, since ξ remains a bounding hyperrectangle in those cases. Note that the output dimensionality d is equal to the number of time steps T over which the HEMS algorithm is solved. Additionally, $\mathbb{1}(\cdot)$ denotes the indicator function. The prediction interval evaluation metrics are formally defined in Eqs. (B.1)–(B.8). To provide a comprehensive assessment of the prediction intervals, we report both marginal metrics (evaluated per time step) and joint metrics (evaluated across the entire prediction horizon).

$$PICP_t = \frac{1}{|\mathcal{D}_{\text{test}}|} \sum_{j=1}^{|\mathcal{D}_{\text{test}}|} \mathbb{1} \left(l_t^{(j)} \leq y_t^{(j)} \leq u_t^{(j)} \right) \quad \forall t \in \mathcal{T} \quad (\text{B.1})$$

$$PICP_{\text{joint}} = \frac{1}{|\mathcal{D}_{\text{test}}|} \sum_{j=1}^{|\mathcal{D}_{\text{test}}|} \mathbb{1} \left(y^{(j)} \in \mathcal{B}_{\xi}^{(j)} \right) \quad (\text{B.2})$$

$$MPIW_t = \frac{1}{|\mathcal{D}_{\text{test}}|} \sum_{j=1}^{|\mathcal{D}_{\text{test}}|} \left(u_t^{(j)} - l_t^{(j)} \right) \quad \forall t \in \mathcal{T} \quad (\text{B.3})$$

$$MPIW_{\text{joint}} = \frac{1}{T} \sum_{t \in \mathcal{T}} MPIW_t \quad (\text{B.4})$$

$$LPenalty_t(\alpha) = \frac{1}{|\mathcal{D}_{\text{test}}|} \sum_{j=1}^{|\mathcal{D}_{\text{test}}|} \frac{2}{\alpha} \left[l_t^{(j)} - y_t^{(j)} \right] \cdot \mathbb{1} \left(y_t^{(j)} \leq l_t^{(j)} \right) \quad \forall t \in \mathcal{T} \quad (\text{B.5})$$

$$UPenalty_t(\alpha) = \frac{1}{|\mathcal{D}_{test}|} \sum_{j=1}^{|\mathcal{D}_{test}|} \frac{2}{\alpha} \left[y_t^{(j)} - u_t^{(j)} \right] \cdot \mathbb{1} \left(u_t^{(j)} \leq y_t^{(j)} \right) \quad \forall t \in \mathcal{T} \quad (\text{B.6})$$

$$IS_t(\alpha) = \frac{1}{|\mathcal{D}_{test}|} \sum_{j=1}^{|\mathcal{D}_{test}|} (MPIW_t + LPenalty_t + UPenalty_t) \quad \forall t \in \mathcal{T} \quad (\text{B.7})$$

$$IS_{joint}(\alpha) = \frac{1}{T} \sum_{t \in \mathcal{T}} IS_t \quad (\text{B.8})$$

PICP quantifies the proportion of ground-truth values that fall within the predicted intervals, as defined in Eqs.(B.1) and (B.2). It serves as an empirical estimate of the coverage probability, especially as the size of the test dataset \mathcal{D}_{test} approaches infinity. While PICP evaluates the reliability of the intervals, it does not account for their width. This aspect is captured by MPIW, which measures the average width of the prediction intervals and reflects their sharpness, as shown in Eqs.(B.3) and (B.4). Lower MPIW indicates narrower intervals and, consequently, greater confidence in the predictions.

However, MPIW alone does not indicate whether the prediction intervals successfully contain ground-truth values. To overcome this limitation, the IS metric is introduced, as defined in Eqs.(B.7) and (B.8). This metric combines the average interval width with explicit penalties for violations, where the ground-truth falls below the lower bound or above the upper bound of the interval, as described in Eqs.(B.5) and (B.6), respectively. In doing so, IS provides a more comprehensive evaluation of interval quality. By analysing these metrics together, we gain a clearer understanding of how accurate, sharp, and reliable the predicted intervals are.

In addition to the traditional prediction interval metrics described above, we also evaluate the frequency of overbid, defined as the proportion of intervals per day in which the true value of up-regulation flexibility $y_t^{(j)}$ falls below the lower bound $l_t^{(j)}$ of the predicted interval. This metric is formalised in Eq. (B.9), which quantifies how often the predicted lower bound $l_t^{(j)}$ fails to capture the actual flexibility value, effectively representing instances where the aggregator might have overbid in the mFRR capacity market.

$$\text{Frequency of overbid} = \frac{1}{T} \sum_{t \in \mathcal{T}} \mathbb{1} \left(y_t^{(j)} < l_t^{(j)} \right), \quad (\text{B.9})$$

This concept was originally introduced in [8] to assess compliance with the P90 requirement mandated by Energinet, which stipulates that at least 90% of the time, the actual flexibility should lie above the bid level. Hence, the mean frequency of daily overbid should remain below 10% for our probabilistic forecast model to qualify for market participation. This requirement ensures that the aggregator does not systematically overestimate its capacity, thereby supporting reliable and secure market operations.